Contents lists available at ScienceDirect



Surface & Coatings Technology

journal homepage: www.elsevier.com/locate/surfcoat



Synthesis of hexagonal boron nitride nanocoatings for corrosion prevention of iron substrates

Venkata A.S. Kandadai ^{a,c}, Jacob B. Petersen ^a, Venkataramana Gadhamshetty ^{b,c}, Bharat K. Jasthi ^{a,c,*}

- a Department of Materials and Metallurgical Engineering, South Dakota School of Mines & Technology, 501 East Saint Joseph St, Rapid City, SD 57701, USA
- b Department of Civil and Environmental Engineering, South Dakota School of Mines & Technology, 501 East Saint Joseph St, Rapid City, SD 57701, USA
- ^c 2-Dimensional Materials for Biofilm Engineering, Science and Technology (2D-BEST) Center, South Dakota School of Mines & Technology, 501 East Saint Joseph St, Rapid City, SD 57701, USA

ARTICLE INFO

Keywords: Hexagonal boron nitride Thin films Nanocoatings Corrosion Direct growth Pulsed laser deposition

ABSTRACT

Iron and its alloys have applications in diverse fields such as civil infrastructure, aerospace, and defense. Corrosion of these alloys in saline environments is a significant concern that causes huge environmental losses. The current study explores pulsed laser deposition technique to synthesize hexagonal boron nitride (hBN) films as protective coatings, directly on iron (Fe), to mitigate the corrosion. Microstructural, mechanical, wetting, and corrosion properties of hBN-coated Fe substrates were investigated at different deposition temperatures (25–800 °C) and varying thicknesses (35–115 nm). Raman spectra and transmission electron microscopy confirmed the presence of hBN in as-deposited films. Crystallinity and surface roughness of hBN coatings increased as deposition temperature increased. Electrochemical studies performed in 3.5 wt% NaCl solution showed that the 115 nm thick hBN coatings deposited at 600 °C resulted in lower corrosion rates and has \sim 6-fold higher corrosion resistance than bare Fe. Also, the corrosion rates decreased with an increase in hBN coating thickness. Overall results suggest that hBN nanocoatings reduced the corrosion activity and can potentially serve as a corrosion-resistant barrier coatings in saline environments.

1. Introduction

Owing to the ubiquitous use of iron alloys in diverse components related to aerospace, civil infrastructure (e.g., bridges, pipelines), defense, and medical applications [1], iron (Fe) alloys account for nearly 95 % of metal production globally [2]. Although iron substrates remain stable under pristine and neutral pH conditions, they are vulnerable to corrosion when exposed to aggressive environments (e.g., acidic and salty conditions). Such corrosion issues cause structural failures and reduce service lifetime of iron components [3,4]. Furthermore, corrosion issues have been attributed to leaks and spills in iron containers and pipelines that can result in negative environmental impacts [4]. Thus, corrosion management practices are critical to sustain the functions of any modern society. An effective way of protecting metallic components and structures is by applying protective coatings on surfaces, which can inhibit electrochemical reactions and mitigate corrosion processes. These coatings are typically based on polymers [5-9] and their composites [10-13] and ceramic material [14-17]. While these coatings offer certain benefits, they are not necessarily suitable for protecting iron substrates, especially when exposed to aggressive conditions (e.g., marine environment). Polymer coatings have been reported to be prone to wear and mechanical degradation in aggressive conditions [11]. Their high profile thickness (50–1000 μ m) can disrupt functionalities of underlying metal surfaces. Furthermore, their inherent characteristics (e.g., porous microstructure and hydrophilicity) facilitate permeation of corrosive species (e.g., metal ions) onto underlying surfaces [11,18].

Thermochemical treatments such as carburizing, boriding, nitriding, titanizing, chromizing, vanadizing and niobizing has also been used to modify the surfaces for improving the tribological and corrosion properties of steels [19]. These treatments form boride, nitride or carbide layers as coating on the material surface which alters their mechanical, wear and corrosion properties [19–22]. For example, Günen et al. [21] used three different thermochemical coatings on steel and showed that boride coated steel can be used as an alternative to expensive alloys such as Monel, Inconel, and Hastealloy in nuclear power plants. Though it is proven that corrosion resistance of steels improved by these coatings,

^{*} Corresponding author at: 501 East Saint Joseph St, Rapid City, SD 57701, USA. E-mail address: Bharat.Jasthi@sdsmt.edu (B.K. Jasthi).

they have limitations in terms of requirements for higher process temperatures, surface preparation, hazardous gas generation, and long processing times [19,23]. Some thermochemical coatings can also degrade at higher temperatures due to diffusion of coating elements into the substrate resulting in undesired phase formation. Moreover, the sensitization might arise in stainless steels resulting in the precipitation of chromium carbides or nitrides which deteriorate the corrosion properties [24].

A new class of nanometer thick, protective coatings based on building blocks of two-dimensional (2D) materials can alleviate some of the above challenges. Graphene materials have been widely explored for corrosion applications in the last decade [25-28], and demonstrated outstanding barrier properties and resistance to both biotic and abiotic forms of corrosion. However, if improperly designed, graphene coatings can aggravate corrosion of underlying metals. Their high electrical conductivity and presence of any inherent defects in graphene coatings can promote galvanic corrosion of underlying metals [29-31]. In our earlier studies, we demonstrated the use of single and multiple layers of 2D hexagonal boron nitride (hBN) as the thinnest insulating barriers to protect metals under both biotic and abiotic conditions [32,33]. Such hBN coatings offer excellent oxidation resistance in presence of harsh chemicals, high temperatures, and detrimental microorganisms [32–39]. Furthermore, it is a compelling choice for electronic industries [40–44] because of its insulating properties (wide bandgap of 6–6.5 eV), and thermal conductivity.

Majority of the recently explored hBN coatings have been obtained using chemical vapor deposition (CVD) [34,45-49] and physical vapor deposition (PVD) [3,36-38,50-53] techniques. CVD and PVD methods also showed an ability to produce large-area, continuous hBN films with better uniformity, and they proved to be effective long-term durable coatings for corrosion resistance applications [38,45,49-51]. The disadvantages of CVD methods lie in terms of use of higher temperatures, toxic gases, slower growth rates, and limited to few substrates. Whereas physical vapor deposition (PVD) techniques use plasma to produce hBN films on diverse range of substrates at lower temperatures with higher deposition rates without the use of toxic gases. Therefore, this study uses the pulsed laser deposition (PLD) technique (one of the PVD methods) to deposit hBN thin films. In the PLD technique, a high-energy laser beam is directed at target, where atoms from surface of the target evaporate in the form of a plume and condense onto substrates, where subsequent film growth occurs [54]. PLD technique has been successfully employed to deposit a wide range of thin films for various applications at relatively lower temperatures [55–60].

Nanocoatings of hBN were successfully synthesized using PVD techniques and the results showed an improvement in the corrosion properties when deposited on stainless steel (SS) substrates [3,36–38,50–53]. For example, Kumar et al. [36] have demonstrated the use of PLD process for obtaining micron-thick hBN films on SS substrates. Magnetron sputtering (a method of PVD) technique was used by Tang et al. [38] and Singh et al. [37] for depositing 200 nm and 750 nm thick hBN thin films on SS substrates. While hBN nanocoatings on SS substrates showed improved corrosion resistance, the effectiveness of these coatings on pure Fe substrates has not been explored. Additionally, a knowledge gap exists regarding the impact of deposition temperature and thickness of hBN coatings on their microstructure, mechanical, and corrosion properties. So, in this work, broad temperature range was selected from room temperature 25 $^{\circ}\text{C}$ to 800 $^{\circ}\text{C}$, which is below the temperature range of hBN synthesis using CVD, to assess the quality of hBN coatings on microstructure and the resultant corrosion properties.

The current study focuses on using PLD as a nanoscale manufacturing method for obtaining protective corrosion resistant hBN coatings directly on Fe substrates. The primary goal of this research is to investigate the effects of deposition temperatures on the film microstructure and its related corrosion properties of hBN coatings on Fe substrates. Microstructural characterization was carried out, as well as the effects of deposition temperature (25 $^{\circ}$ C, 300 $^{\circ}$ C, 600 $^{\circ}$ C, and 800 $^{\circ}$ C) on wetting,

corrosion, and mechanical properties were explored. Moreover, the influence of hBN coating thickness (35 nm, 65 nm, and 115 nm) on corrosion properties of Fe substrates was also examined.

2. Experimental procedure

2.1. Synthesis of hBN nanocoatings

The substrates used for hBN deposition were double-sided mirrorfinished 99.5 % pure Fe discs (50 mm diameter and 0.9 mm thickness). These substrates were ultrasonically cleaned in acetone, followed by methanol for 15 min. The chemical composition of Fe substrates was determined using X-ray fluorescence (XRF), which is shown in the supplementary information, Table S1. A PLD system (248 nm Krypton Fluoride (KrF) excimer laser) was used to synthesize hBN nanocoatings on cleaned Fe substrates. The target used for the deposition was 99.5 % pure hBN with dimensions of 50.8 mm in diameter and 6.35 mm in thickness. The target was rotated at 30 RPM, and substrate was rotated at 10 RPM during the hBN deposition. The target was pre-ablated for 15 min before each deposition to remove unwanted impurities from the surface. Substrate was then heated to the preferred deposition temperature, such as 25 °C, 300 °C, 600 °C, and 800 °C. In the first set of samples, hBN deposition onto Fe substrates was carried out for 90 min at the temperatures mentioned above. In the second set of samples, the deposition temperature was maintained at 600 °C, and depositions were performed for 15 min, 45 min, and 90 min to achieve a thickness of 35 nm, 65 nm and 115 nm. Table 1 lists the process parameters for hBN thin film deposition on Fe substrates. The schematic representation of the PLD process and deposition of hBN thin films on Fe substrate are shown in Fig. 1a and b.

2.2. Characterization of hBN nanocoatings

In-situ ellipsometry was used to measure the thickness of deposited hBN thin films. Optical parameters of the Fe substrate (prior to hBN deposition) were measured, and a suitable model was constructed using FS-1 software, which was later used for measuring final thickness of deposited hBN coatings. Raman Microscope (XploRA plus) was employed to determine the phases in as-deposited coatings. Five spectra from each sample were collected, and the mean Raman peak frequency with standard deviation was reported. Crystallinity and interplanar spacing of deposited hBN nanocoatings were examined using selective area electron diffraction (SAED) patterns and imaging using a transmission electron microscope (TEM) (JEM-2100 LaB₆).

A scanning electron microscope (SEM) (ThermoScientific Helios 5 CX) was utilized to evaluate the microstructure of as-deposited hBN nanocoatings. The focused ion beam (FIB, source-Gallium), equipped with SEM, was utilized for two purposes: one was to prepare TEM samples by performing a FIB lift-out process, and the other was to mill the sample to view cross-sections of the hBN/Fe to measure film thickness and compare with ellipsometry data. Before using FIB, a tungsten

 Table 1

 PLD process parameters used for hBN thin film deposition.

r r	F		
Process parameter	Value		
Target	hBN		
Substrate	Fe		
Substrate to Target distance	96 mm		
Laser source	KrF (248 nm)		
Laser Energy	350 mJ		
Laser frequency	10 Hz		
Background pressure	$1.3\times10^{-5}~\text{mT}$		
Deposition pressure	5 mT		
Atmosphere (gas)	Ar:N ₂ (1:1)		
Deposition time	15 min, 45 min, 90 min		
Deposition temperature	25 °C, 300 °C, 600 °C, 800 °C		

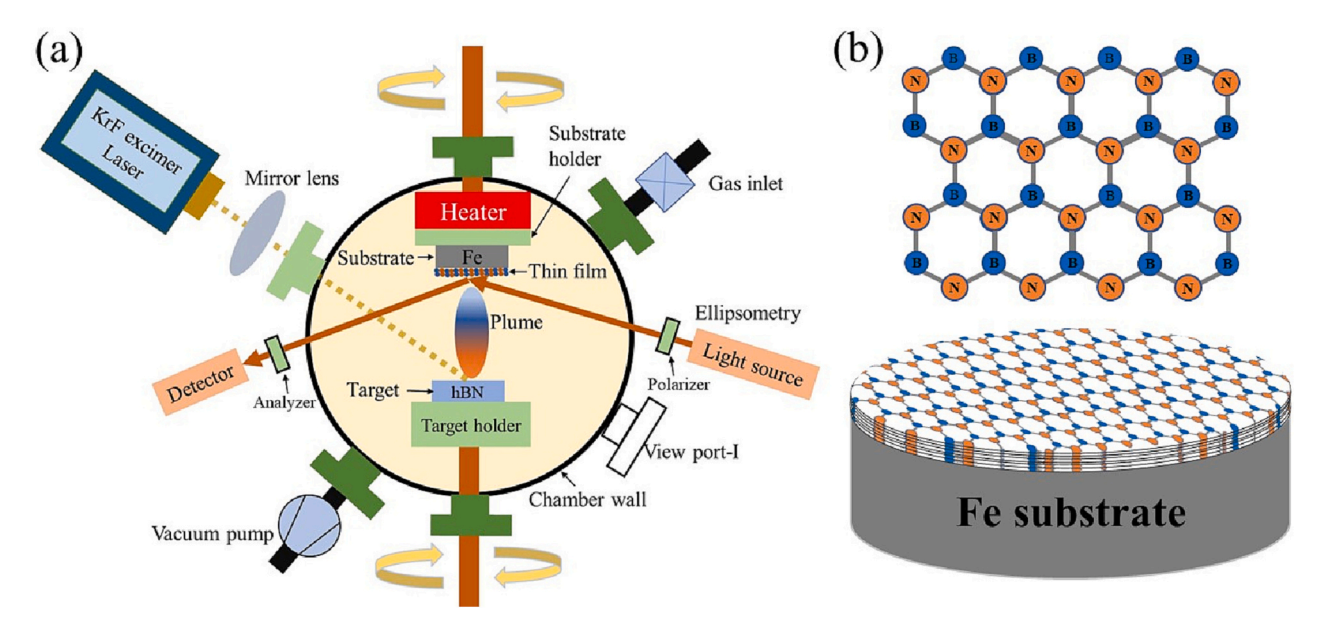


Fig. 1. Schematic representation of the thin film deposition process showing: (a) PLD technique to deposit hBN nanocoating; and (b) a layer of hBN and hBN nanocoating deposited on Fe substrate (hBN/Fe).

cap was applied in-situ to the area of interest to prevent FIB damage to the film during milling. Compositional analysis of hBN coatings in asdeposited and post-corrosion conditions was performed using energy dispersive spectroscopy (EDS) using an Oxford Ultim Max EDS detector and Aztec 5.1 analysis software. Grazing incidence X-ray Diffraction (GIXRD) analysis was performed to identify the phases present in the thin films. GIXRD analysis was performed at an incident angle of 2°, and the JADE 8.5 program was utilized to analyze the diffraction data. MTS nanoindenter XP system was employed to assess the mechanical properties of deposited films with a Bercovich indenter tip. A minimum of thirty nanoindenter measurements per sample were measured. These were produced as load vs. displacement curves, from which the hardness and modulus were calculated using the Oliver-Pharr method [61,62]. For the indentation measurements, a depth limit of 15 nm, strain rate of 0.04 s^{-1} , a peak hold time of 15 s, and Poisson's ratio of 0.211 [63,64] were used for hBN nano coatings. Whereas for bare Fe substrate, a maximum load of 5 mN, time to load of 15 s, a peak hold time of 10 s, and Poisson's ratio of 0.291 [65] were used. The hardness and modulus were determined using the Testworks4 application.

Surface roughness of hBN coatings was evaluated using a Bruker MultiMode 8 atomic force microscope (AFM) with a ScanAsyst-Air cantilever with a tip radius of ~2 nm. Nanoscopeanalysis V1.6 software was used to estimate surface roughness of coatings in terms of root mean square height (Rq). The rougher surface of the Fe substrate made it challenging to measure surface roughness of hBN coatings. Therefore, hBN was deposited on polished silicon substrates (referred to as hBN/Si) to measure the roughness of as-deposited thin films at different deposition temperatures. Wettability of thin films was evaluated using a goniometer (Rame-Hart Model 500 goniometer/tensiometer). 10 µL water drops were used to measure contact angle. Five contact angle measurements (or drops) were made on each sample, and each drop was measured ten times. Mean values of the contact angle of hBN coated and uncoated Fe substrates with standard deviation were presented. The corrosion behavior of the prepared coatings and the Fe substrate was examined by potentiodynamic polarization and electrochemical impedance spectroscopy (EIS) using a Gamry potentiostat Reference 600+. The electrochemical cell (Ametek K0235-flat cell) with a threeelectrode system was used, where the reference electrode is Ag/AgCl, the counter electrode is platinized aluminum mesh, and the working electrode is either hBN/Fe or Fe substrate. The electrolyte used for measurements was 3.5 wt% NaCl solution, and all measurements were

performed at room temperature. 1 cm² sample area was exposed to the electrolyte solution, and four measurements per sample were collected. Open circuit potential (OCP) was recorded for 60 min for all samples prior to EIS and Tafel tests to attain equilibrium potential. EIS tests were performed at the OCP in the frequency range of 10,000 Hz to 0.01 Hz using an AC signal amplitude of ± 10 mV. Following EIS, Tafel tests were performed and recorded with a potential sweep of ± 250 mV vs. OCP with a scan rate of 0.167 mV/s. Gamry Echem Analyst software was utilized to analyze Tafel and EIS plots to determine corrosion parameters of the samples.

3. Results and discussion

3.1. Thickness measurements of hBN thin films

The thickness of hBN thin films at different deposition temperatures and deposition times were determined using in-situ ellipsometer. The final thickness of hBN films was measured for 120 s by rotating the substrate, as shown in Fig. 2a (raw ellipsometric data), and the average thickness with standard deviation was reported. Raw ellipsometric data of all deposited coatings were represented in the supplementary information, Fig. S1. Fig. 2b shows the final thickness of hBN/Fe deposited at various deposition temperatures with 90 min deposition period. The results showed that the average thickness of hBN films was found to be 114–124 nm. There has been a slight decrease in film thickness (\sim 5–10 nm) observed with increase in deposition temperature from 25 °C to 300 °C and higher, which can be attributed to thermal energy causing increased mobility of adatoms at higher temperatures resulting in films with compact, denser and fewer defects [66,67]. Fig. 2c shows the thickness of hBN coatings deposited at 600 °C as a function of deposition time. Results suggested that with the increase in deposition time, the thickness of hBN films increased from 35 nm for 15 min to 65 nm for 45 min and 115 nm for 90 min, respectively.

Cross-sectional image analysis of as-deposited hBN nanocoatings was performed by milling the sample using FIB to confirm ellipsometric thickness measurements. SEM cross-section micrographs (post FIB milling) of hBN coatings deposited at 600 °C for 90 and 45 min deposition times are shown in Fig. 3 and micrographs for 15 min deposition time are shown in supplementary information, Fig. S2. The thickness measured from cross-sectional image analysis of hBN/Fe deposited at 600 °C for 90 min is $\sim\!110$ nm, and for 45 min is $\sim\!62$ nm (as shown in

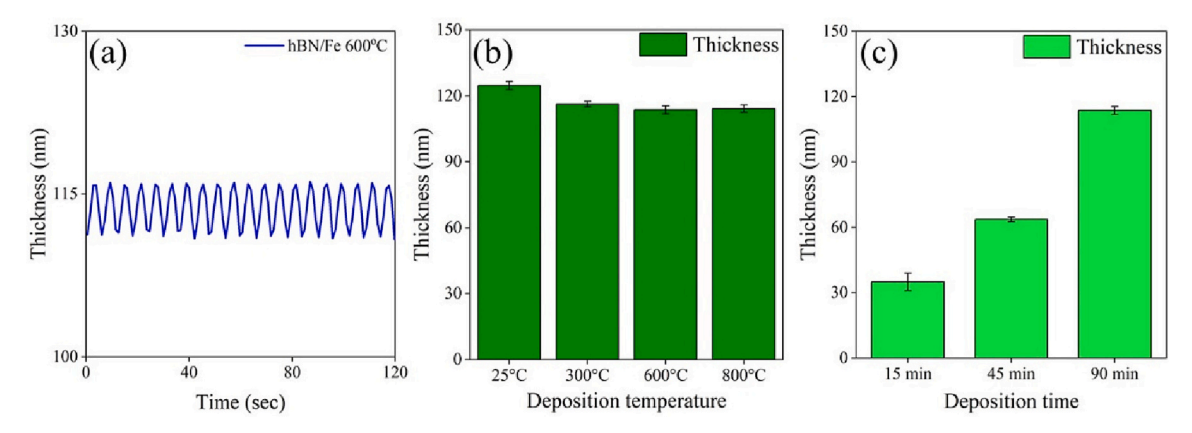


Fig. 2. Thickness measurements of hBN coatings using in-situ ellipsometry showing: (a) raw data of hBN/Fe deposited at 600 °C; (b) thickness of hBN films deposited for 90 min at different deposition temperatures; and (c) thickness of hBN films deposited at 600 °C for different deposition times.

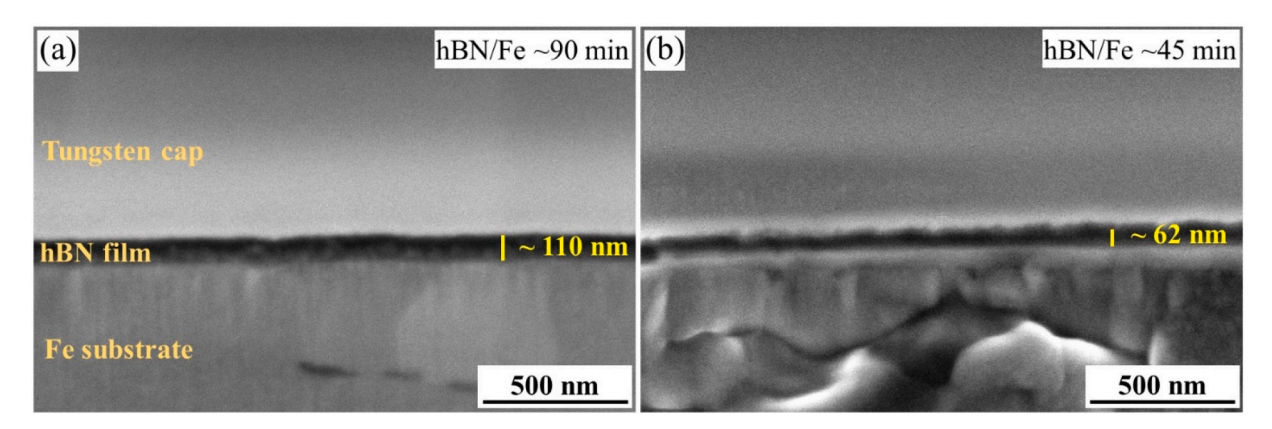


Fig. 3. Post-FIB SEM cross-section micrographs showing thickness of hBN nanocoatings deposited at 600 °C: (a) hBN/Fe deposited for 90 min; and (b) hBN/Fe deposited for 45 min.

Fig. 3a,b). Therefore, thickness measured from FIB/SEM cross-section images showed an excellent consistency with the measurements determined using in-situ ellipsometry data shown in Fig. 2b,c.

3.2. Characterization of hBN nanocoatings

The phases present in as-deposited coatings were detected using Raman spectroscopy. The Raman signatures reported for crystalline hBN is $\sim\!1366~\text{cm}^{-1}$ [68], a first-order Raman peak (arising from E_{2g}

symmetry vibrational phonon mode). This peak frequency is observed in all the deposited coatings investigated in this study, confirming the presence of a hexagonal crystallographic structure of boron nitride. The Raman spectral data of all deposited coatings are shown in the supplementary information, Fig. S3. Using the *OriginPro 2023 (64-bit)*, the Lorentzian function is utilized to fit the raw Raman spectra (as shown in Fig. 4a), which provides the peak center location. Fig. 4b shows the Raman signatures of hBN phase in coatings deposited for 90 min at various deposition temperatures. It is evident from Fig. 4b that the mean

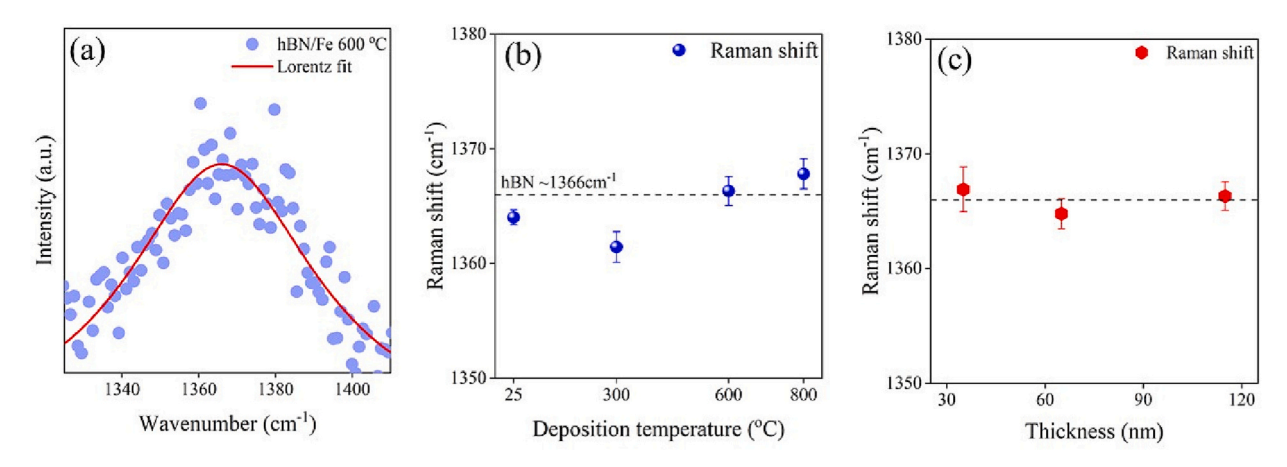


Fig. 4. Raman spectra of hBN nanocoatings showing: (a) Raw Raman spectrum fitted with Lorentzian function of hBN/Fe deposited at 600 °C for 90 min; (b) Raman shifts of hBN/Fe deposited for 90 min at various deposition temperatures; and (c) Raman shifts of hBN/Fe deposited at 600 °C as a function of thickness.

Raman peak frequencies in the range of 1362–1367 cm⁻¹ confirmed the presence of hexagonal phase BN in all the depositions. The reported literature [38,50–53,69,70] of Raman analysis of hBN thin films also shows peak frequencies in the range of 1363–1374 cm⁻¹, which is consistent with our data.

Fig. 4c indicates the Raman shifts of hBN coatings deposited at 600 $^{\circ}\text{C}$ as a function of thickness. The results also confirm the presence of hexagonal BN as Raman shifts of these thin films were in the range of 1364–1366 cm^{-1} , closely matching the crystalline hBN Raman signature. The overall results suggest that hBN films deposited at 600 $^{\circ}\text{C}$ show a close match of Raman peak frequency with crystalline hBN compared to other thin films made at different deposition temperatures. Also, almost no considerable change in Raman shifts was observed for hBN coatings of various thicknesses deposited at 600 $^{\circ}\text{C}$.

The crystallinity of hBN coatings deposited on Fe substrates was examined using high resolution TEM (HRTEM) images and SAED patterns. The FIB lift-out sample used for TEM analysis is shown in Supplementary information, Fig. S4. Fig. 5 shows HRTEM images and SAED patterns (shown as an inset at the top right corner) of hBN/Fe depositions at different deposition temperatures. The HRTEM microstructures in Fig. 5 confirms the nanosheets/nanocrystals of hBN, with an interplanar spacing of 0.30–0.35 nm, and is consistent with the literature [36,71]. The hBN films grown on these substrates have shown polycrystalline nature, exhibiting different crystallographic orientations at all deposition temperatures, as evident from diffraction rings in SAED patterns in Fig. 5. The crystallinity of hBN coatings increased with

deposition temperature as the nanocrystallites of hBN are more uniform at deposition temperatures ${\ge}600~^{\circ}\text{C}$. At the deposition temperatures of 25 $^{\circ}\text{C}$ and 300 $^{\circ}\text{C}$, hBN coatings consisted of nanocrystallites (yellow circles in Fig. 5a, b) with amorphous regions (red circles in Fig. 5a, b). Deposition temperatures of 600 $^{\circ}\text{C}$ and above resulted in a homogeneous distribution of hBN nanocrystallites with fewer amorphous regions due to increased surface diffusion and mobility of adatoms.

The SAED pattern of the hBN thin film deposited at 25 °C showed a highly textured (001) and (100) planes. As deposition temperature increased to 300 °C, the (112) oriented grains started to grow with the addition of strong textured (001) and (100) planes. At higher deposition temperatures of 600 °C and 800 °C, texture diminished; the nanocrystallites uniformly started to grow, and hBN thin films consisted of (002), (100), and (110) planes. Raman spectra results (shown in Fig. 4) are consistent with TEM analysis, which showed the hexagonal crystallographic orientation of as-deposited BN thin films. Therefore, the overall TEM analysis suggested that thin films deposited at temperatures \geq 600 °C showed a uniform distribution of nanocrystallites of hBN with small fractions of amorphous regions.

Grazing incidence X-ray diffraction (GIXRD) was also carried out to identify the phases present in the deposited coatings. GIXRD analysis was performed on Si (100) substrates because the high-intensity peak of iron substrate at 2θ of 55° was observed, which diminished the other hBN peaks. GIXRD pattern of hBN coatings deposited on Si substrates as a function of deposition temperature are shown in supplementary information, Fig. S6 and confirms the presence of hBN phase in all the

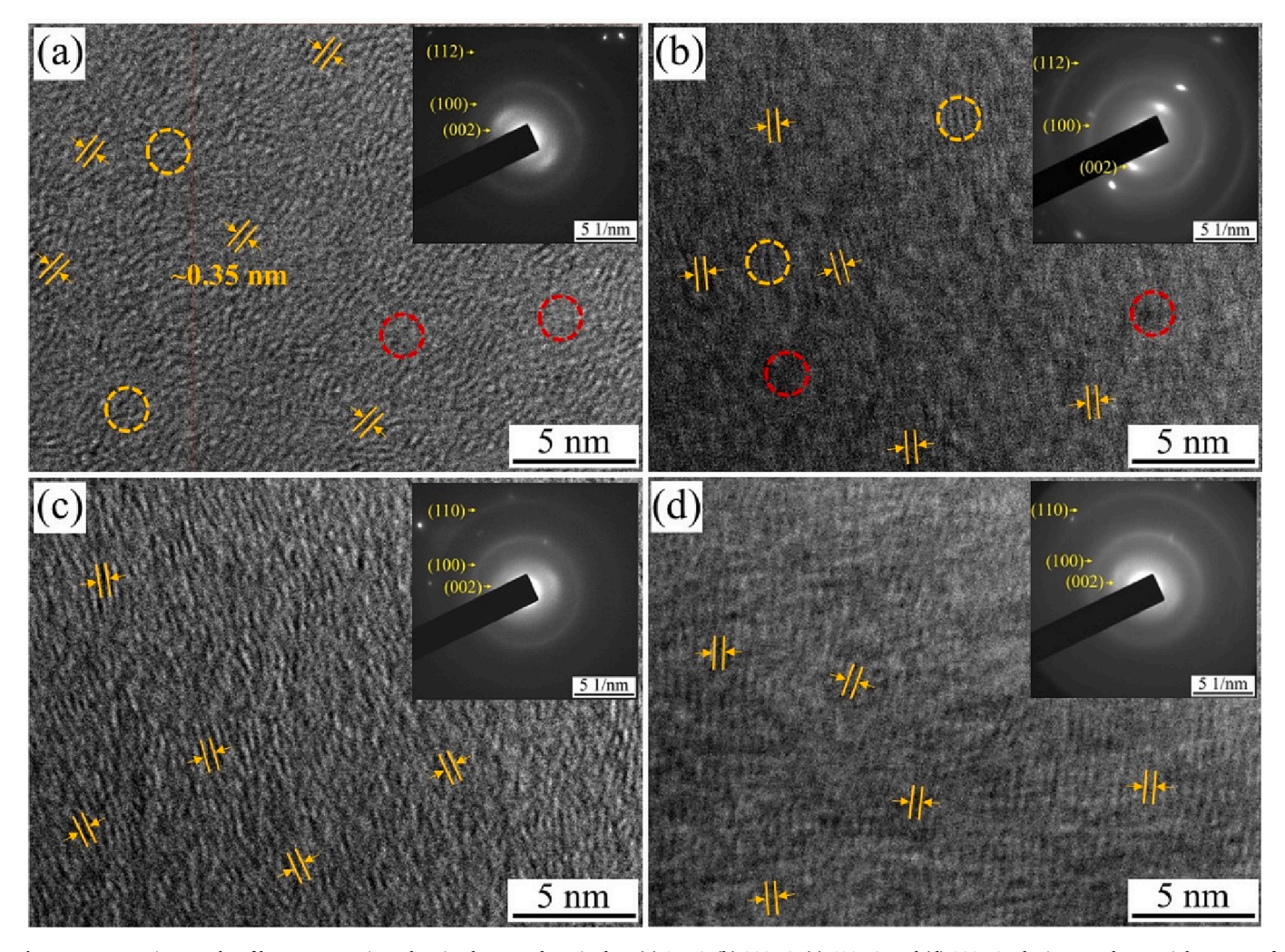


Fig. 5. HRTEM micrographs of hBN nanocoatings showing hBN/Fe deposited at: (a) 25 °C; (b) 300 °C; (c) 600 °C; and (d) 800 °C. The inset at the top right corner of micrographs shows the SAED patterns of respective hBN thin films.

coatings. However, at low deposition temperatures of 25 °C and 300 °C, multiple diffraction peaks (one diffraction peak observed at $\sim\!65^\circ$) are not observed due to amorphous nature of coatings (as shown in Fig. 5a, b). With the increase in deposition temperature, the intensity of 65° peak increased and additional peaks started to show for hBN/Fe at 600 °C and 800 °C at 20 of $\sim\!35^\circ$ and $\sim\!48^\circ$, respectively. This again can be attributed to increased nanocrystallite distribution with less amorphous regions, as evident from TEM results, Fig. 5c,d. GIXRD data confirm the presence of polycrystalline hBN, which also matches with the TEM analysis. The overall characterization with Raman spectroscopy, TEM and GIXRD analysis confirms the presence of hexagonal BN phase in the deposited coatings.

SEM analysis was performed to observe the surface morphology of hBN coated and uncoated Fe substrates. Fig. 6 shows SEM microstructure of hBN/Fe substrates deposited for 90 min at various deposition temperatures. Fig. 7 shows SEM micrographs of hBN/Fe deposited at 600 °C with different thicknesses. As shown in Figs. 6 and 7, the microstructure of hBN coatings clearly depends on the deposition temperature and thickness. Large hBN particulates ranging from 30 to 200 nm are found in the microstructures (indicated by yellow arrows in Figs. 6b-e and Figs. 7a-c) of all deposited thin films, and EDS analysis (shown in supplementary information Fig. S7) confirmed these particulates as BN with a few particulates being slightly B rich. These particulate formations are frequently observed and regarded as one of the drawbacks of PLD process [52,72]. Fig. 6a shows the micrograph of an Fe substrate before hBN film deposition. The surface of the Fe substrate appears to be slightly rough (most likely from the polishing process), and the microstructure of the hBN nanocoatings at all deposition temperatures and thicknesses almost mirrored the surface of the Fe substrate, as evident from Figs. 6b-e and Figs. 7a-c.

The microstructure of hBN/Fe made at 25 °C (shown in Fig. 6b) seems to exhibit layer-by-layer growth. This is because the poor surface adatom mobility causes a layered growth structure when $T_s < (10\ \%)\ T_m$ (T_s is substrate temperature, T_m is melting point of the film), which is explained by the structure zone models (SZM) [73,74]. The primary mode of thin film growth of hBN/Fe depositions made at $\geq 300\ ^{\circ}\text{C}$ seems to be layer plus island growth. As deposition temperature increased to 300 °C, as shown in Fig. 6c, hBN nanoislands began to form. This is due

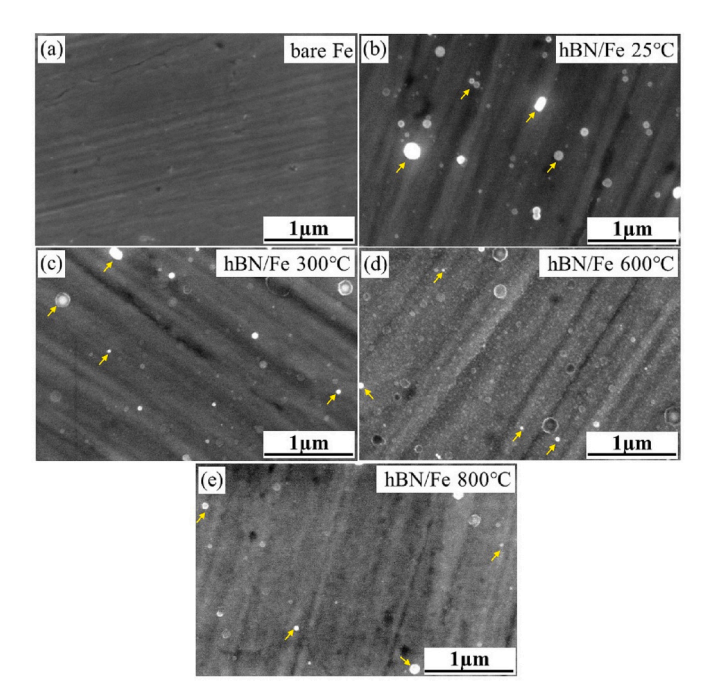


Fig. 6. SEM micrographs of (a) bare Fe; and hBN coated Fe substrates deposited for 90 min at: (b) 25 $^{\circ}$ C; (c) 300 $^{\circ}$ C; (d) 600 $^{\circ}$ C; and (e) 800 $^{\circ}$ C.

to improved surface mobility and diffusion of adatoms when $T_s < (10\text{--}30~\%)~T_m,$ again can be explained by SZM [73,74], leading to nanoisland formation. The nanoisland formation was further increased with rise in the deposition temperature to 600 °C, and the microstructure now appears to be a little coarser, as evident from Fig. 6d, due to enhanced surface adatom mobility and diffusion. At a deposition temperature of 800 °C, the microstructure appears to be similar to that of hBN/Fe made at 600 °C, with the exception that the nanoislands seem to be packed closer together.

The hBN coatings deposited at 25 °C and 300 °C experienced cracking and delamination in some locations on the substrates, as shown in supplementary information Figs. S8, S9. This interfacial delamination of hBN films can be attributed to the thermal stresses [75] developed due to variations in the coefficients of thermal expansion of substrate and film. Though the deposition is carried out at 25 °C and 300 °C, the radiative heating (caused due to plasma and condensation of plasma material on the substrate) developed inside the chamber, and rapid cooling of the substrate (at the rate of 30–40 °C/min during the cooling cycle) might have resulted in thermal stresses at the film/substrate interface [52,76,77]. The hBN depositions made at 600 °C showed good bonding with no delamination or cracking of the films. However, hBN/ Fe deposited at 800 °C showed some cracking tendencies in selected locations (supplementary information, Fig. S10). This could be attributed to lattice strains developed due to lattice mismatch between the hBN film and Fe substrate [33,76-78]. The lattice strains developed due to coarsening of Fe grains at 800 °C may have caused lattice misfit with the hBN film. However, a more detailed TEM analysis is needed to fully understand the growth of hBN films on Fe, and the influence of Fe grain orientation and size.

From Fig. 7, it is evident that with the increase in the thickness of hBN films deposited at 600 °C from 35 nm to 115 nm, the hBN nanoisland formation increases, and the surface appears to be rougher. Almost no nanoisland formation was observed for hBN/Fe deposited with a thickness of 35 nm, which can be attributed to a shorter deposition time. A shorter deposition time means insufficient time for surface diffusion, nucleation, and coalescence of adatoms; hence, nanoisland formation is delayed [76]. The hBN film thicknesses of 65 nm and 115 nm correspond to longer deposition times, 45 min and 90 min, respectively, which resulted in increased surface diffusion of adatoms and subsequent coalescence of nanoislands. Therefore, the hBN/Fe with a thickness of 115 nm (longer deposition time of 90 min) showed higher nanoisland formation, and the microstructure (shown in Fig. 7c) appeared coarser than others (Fig. 7a,b). In the end, the microstructural characterization of hBN nanocoatings seems to mirror the surface morphology of the Fe substrate. Also, the growth of hBN films showed a dependence on deposition temperature and time.

3.3. Mechanical properties evaluation of hBN nanocoatings

The mechanical properties of hBN coatings deposited for 90 min at different deposition temperatures were determined from load vs. displacement curves collected by nanoindentation. The load vs. displacement curves of bare Fe substrate and hBN coatings deposited at various deposition temperatures are shown in the supplementary information, Fig. S11. Fig. 8 shows the mechanical properties of bare Fe substrate and hBN/Fe deposited at various temperatures. The results suggested that hBN thin films had a relatively higher hardness and lower modulus compared to bare Fe substrate. The hardness and modulus of the Fe substrate were 3.5 GPa and 200 GPa, respectively, with an average maximum indentation depth of 250 nm. These values are consistent with the mechanical properties reported in literature by Tomita et al. [79], with a hardness of cold rolled pure iron being 3 GPa, and Cleaves et al. [80] with an elastic modulus of 200 GPa. The indentations were performed with a maximum depth of 13-16 nm (roughly 13 % of the film thickness) to reduce substrate influences on indentation measurements. There were no considerable differences in

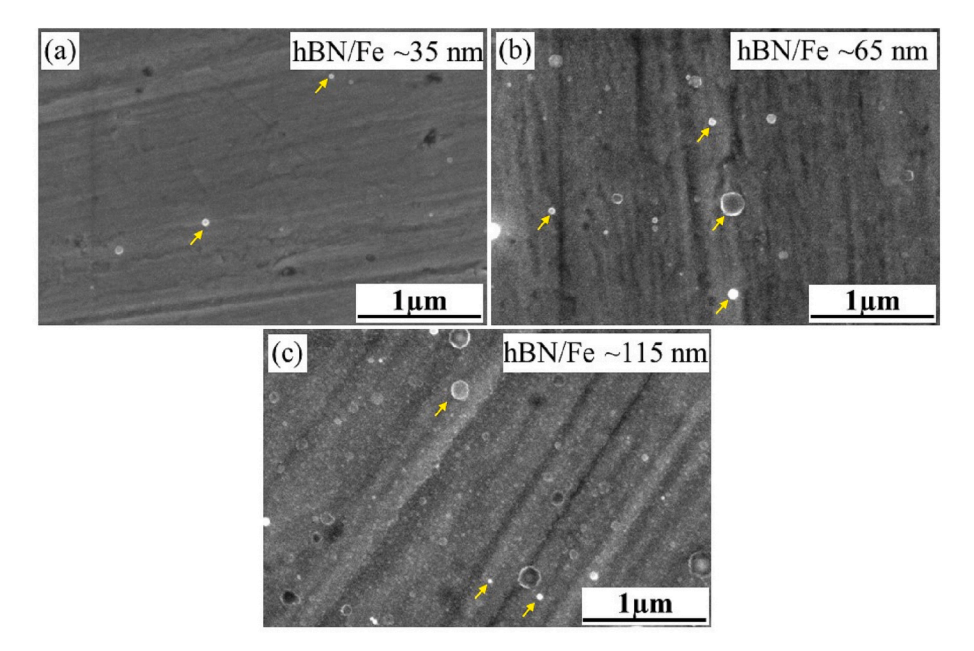


Fig. 7. SEM micrographs of hBN nanocoatings deposited on Fe substrate at 600 °C with different thicknesses of: (a) 35 nm; (b) 65 nm; and (c)115 nm.

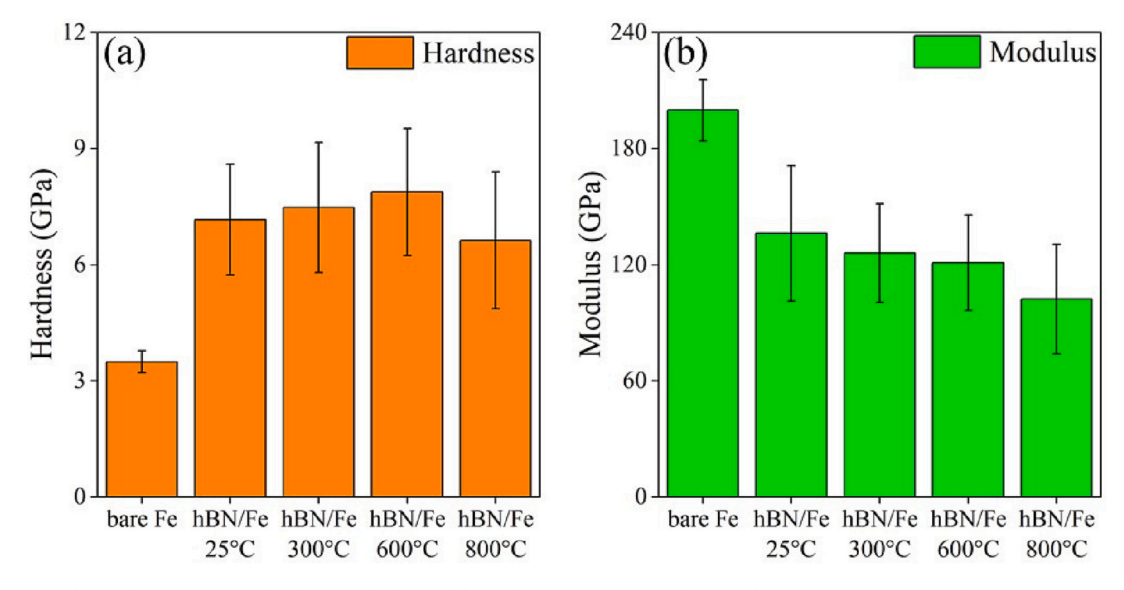


Fig. 8. Mechanical properties (a) hardness and (b) modulus of hBN nanocoatings deposited for 90 min at various deposition temperatures.

hardness and modulus of hBN coatings made at different deposition temperatures, and the values were 7–8 ± 1 GPa and 100–125 \pm 35 GPa, respectively. These values are consistent and similar to previously reported literature [52] of hBN films on silicon substrates by PLD with average hardness and modulus of 10 GPa and 140 GPa. Also, Gocman et al. [81] reported similar results of pulsed laser-deposited hBN coatings on steel substrates with a hardness range of 5–10 GPa and elastic modulus of 95 GPa.

3.4. Surface roughness measurements of hBN nanocoatings

2-dimensional (2D) and 3-dimensional (3D) AFM micrographs of hBN/Si, deposited for 90 min at various deposition temperatures, are presented in Fig. 9. SEM micrographs of hBN/Si are provided in the supplementary information, Fig. S12, and are in good agreement with the surface morphology of hBN on Fe substrates (shown in Fig. 6). The surface roughness of hBN coatings expressed as root mean square height (R_q) , which was determined from AFM topography data. The R_q values

of hBN coatings increased as deposition temperature increased. At a deposition temperature of 25 °C, the hBN/Si showed an R_{q} of 4.0 ± 0.5 nm, which is lower among the deposited thin films. This lower roughness can be attributed to a smoother surface due to the layered growth of hBN films, as shown in Fig. 6b. However, for comparing the roughness data with other deposited films, it was challenging to locate 5 $\mu m \times 5 \, \mu m$ crack-free regions (indicated by black arrows in Fig. 9a) of hBN/Si at 25 $^{\circ}\text{C}.$ The delamination of the hBN coating (indicated by white arrows in 9a) increased the roughness of the coatings. Hence, the roughness values of hBN/Si made at 25 $^{\circ}$ C can still be lower. The R_q increased from 4.0 ± 0.5 nm at 25 °C to 4.8 ± 1.1 nm at 300 °C. This increase in the roughness can be attributed to hBN nanoislands formation starting to begin (as shown in Fig. 6c), making the surface rougher. With further increase in the deposition temperature, R_{q} increased to $6.0{\pm}1.5~\text{nm}$ at $600~^{\circ}\text{C}$ and $6.7\pm0.5~\text{nm}$ at $800~^{\circ}\text{C}$. This is due to enhanced mobility and diffusion of surface adatoms at higher temperatures, leading to more hBN nanoisland formations (as shown in Fig. 6d,e); thus making the surface rougher for the depositions made at 600 °C and 800 °C.

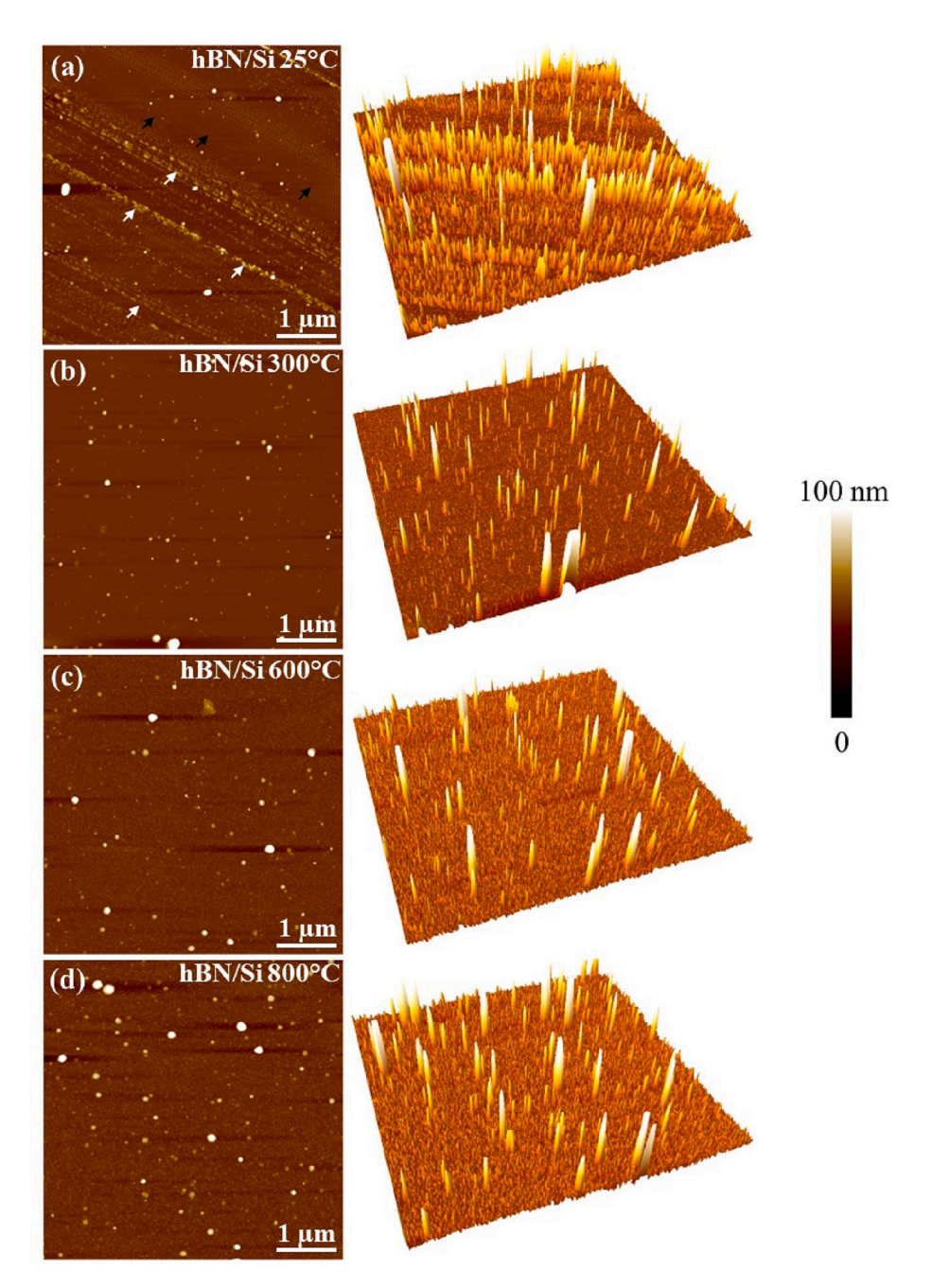


Fig. 9. 2D AFM micrographs and their corresponding 3D images of hBN nanocoatings on Si substrates deposited at: (a) 25 °C; (b) 300 °C; (c) 600 °C; and (d) 800 °C. All images represent the area of 5 μ m \times 5 μ m. The scale bar 0–100 nm is a representation for all the samples.

Fig. 10 shows the AFM micrographs of hBN/Si samples deposited at 600 °C with different deposition times. hBN deposition times 15, 45 and 90 min represents coating thickness of 35, 65 and 115 nm respectively. The results clearly show that the R_q values of hBN coatings increased with the increase in deposition time. At a deposition time of 15 min, the hBN/Si showed an R_q of 2.3 ± 0.2 nm and increased to 5.1 ± 0.2 nm at 45 min and 6.0 ± 1.5 nm at 90 min. This increase in surface roughness matched with the SEM micrographs (shown in Fig. 7) and can be attributed to nanoisland formation. Literature on surface roughness of hBN coatings deposited using PLD have been very limited. Melaibari and Eltaher [82] used femtosecond PLD to deposit BN films on Si substrates (substrate average roughness R_a of 2–3 nm) of thickness 500 nm and showed R_a of 150 nm. Kumar et al. [36] used PLD to deposit 1 μ m hBN films on SS substrates (substrate R_q of 13 nm) and showed R_q of 28 nm. And, literature on the surface roughness of approximately 100 nm thick

hBN coatings was not available to compare our results. Overall, the AFM results suggest that the roughness $\rm R_q$ of as-deposited hBN coatings was in the range of 4–7 nm and the roughness increased with the increase in deposition temperature and thickness.

3.5. Contact angle and wetting properties

The contact angle of hBN coatings at various deposition temperatures and thicknesses is shown in Fig. 11. The results indicate that hBN deposition on Fe substrates increased the wettability compared to bare Fe substrate. The mean contact angle of the bare Fe substrate was 85° , and it was decreased to the range of $54-69^\circ$ with the deposition of hBN coatings at different deposition temperatures. The contact angle of hBN nanocoatings (deposited for 90 min) deposited on Fe substrates increased as deposition temperature increased, as shown in Fig. 11a.

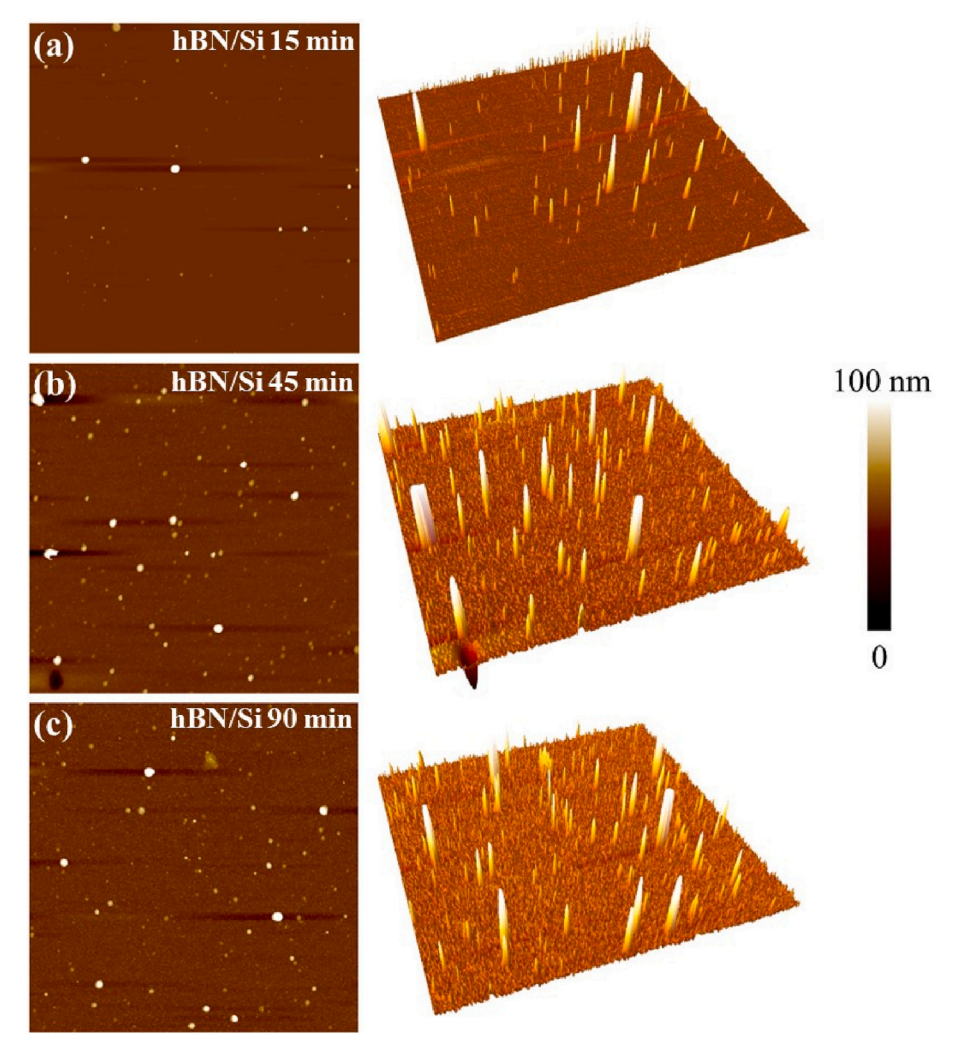


Fig. 10. 2D AFM micrographs and their corresponding 3D images of hBN nanocoatings on Si substrates deposited at 600 °C for various deposition times: (a) 15 min; (b) 45 min; and (c) 90 min. All images represent the area of 5 μ m \times 5 μ m. The scale bar 0–100 nm is a representation for all the samples.

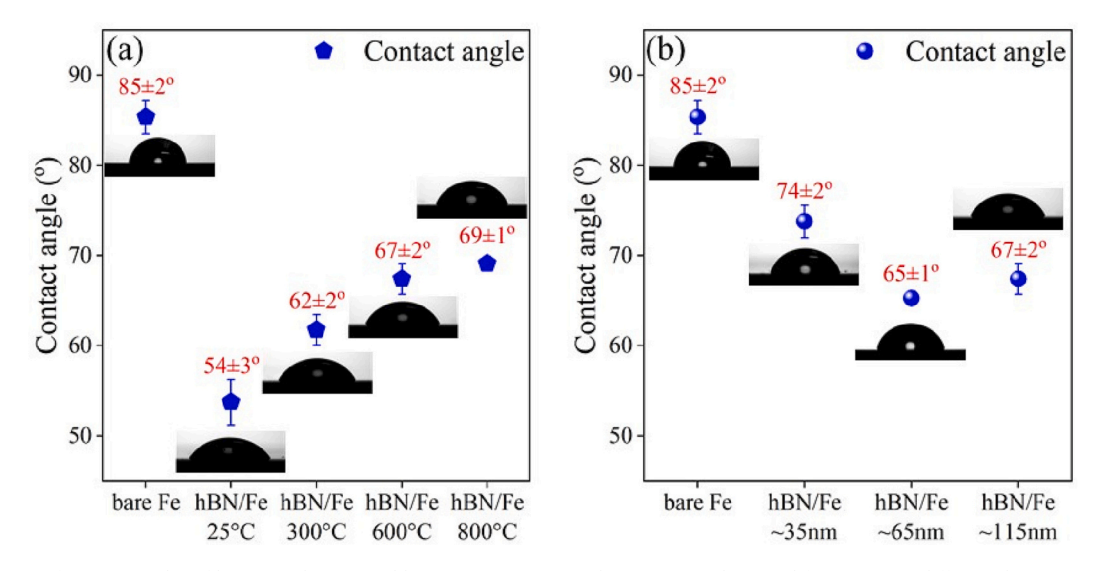


Fig. 11. Comparison of contact angles of bare Fe substrate and hBN nanocoatings: (a) hBN coatings deposited for 90 min at different deposition temperatures; and (b) hBN coatings deposited at 600 °C to various thicknesses. The inset shows water droplet on the respective samples.

This change in the contact angle can be correlated to the surface morphologies of hBN coatings at different deposition temperatures. The Wenzel relation [83] explains the relationship between contact angle and surface roughness: where contact angle scales with surface roughness. Contact angle of hBN/Fe made at $25\,^{\circ}\text{C}$ was $54\pm3^{\circ}$, lowest of all the thin films produced, which can be attributed to lower surface roughness R_q of 4.0 nm. When deposition temperature increased to $300\,^{\circ}\text{C}$, there is a rise in the R_q of 4.8 nm; hence, the contact angle increased to $62\pm2^{\circ}$. The contact angle of coatings was further increased to $67\pm2^{\circ}$ at $600\,^{\circ}\text{C}$ and $69\pm1^{\circ}$ at $800\,^{\circ}\text{C}$ with an increase in their R_q of 6.0 nm and 6.7 nm, respectively.

Wettability of hBN/Fe deposited at 600 °C increased with the increase in film thickness, as evident in Fig. 11b. The mean contact angle of the bare Fe substrate was 85° , and it was reduced to $65–74^\circ$ with the different thicknesses of hBN coatings. The thinnest hBN film (35 nm) on

the Fe substrate showed a relatively higher contact angle $(74\pm2^\circ)$ when compared with thicker hBN coatings. At the deposition time of 15 min, the hBN coating is very thin (~35 nm), and this might not completely cover the grooves/rougher Fe substrate; hence, the contact angle was only dropped to $74\pm2^\circ$. However, with the increase in deposition times, the coatings are thicker, and the contact angle was further reduced to $65-67\pm2^\circ$, and it is most likely that the grooves/rougher Fe substrate is completely covered, and the substrate roughness effect is minimized. The contact angle of hBN nanocoatings reported in the literature was $61-73^\circ$ [84–87] and $44-52^\circ$ for PLD hBN thin films with average roughness R_a of 15 nm [88]. hBN thin films deposited in this study showed a contact angle of $54-74^\circ$, which was in agreement with reported literature. Therefore, the overall results suggest that wettability of hBN films can be correlated to their microstructure and surface roughness. Similar trends have been reported for other thin films

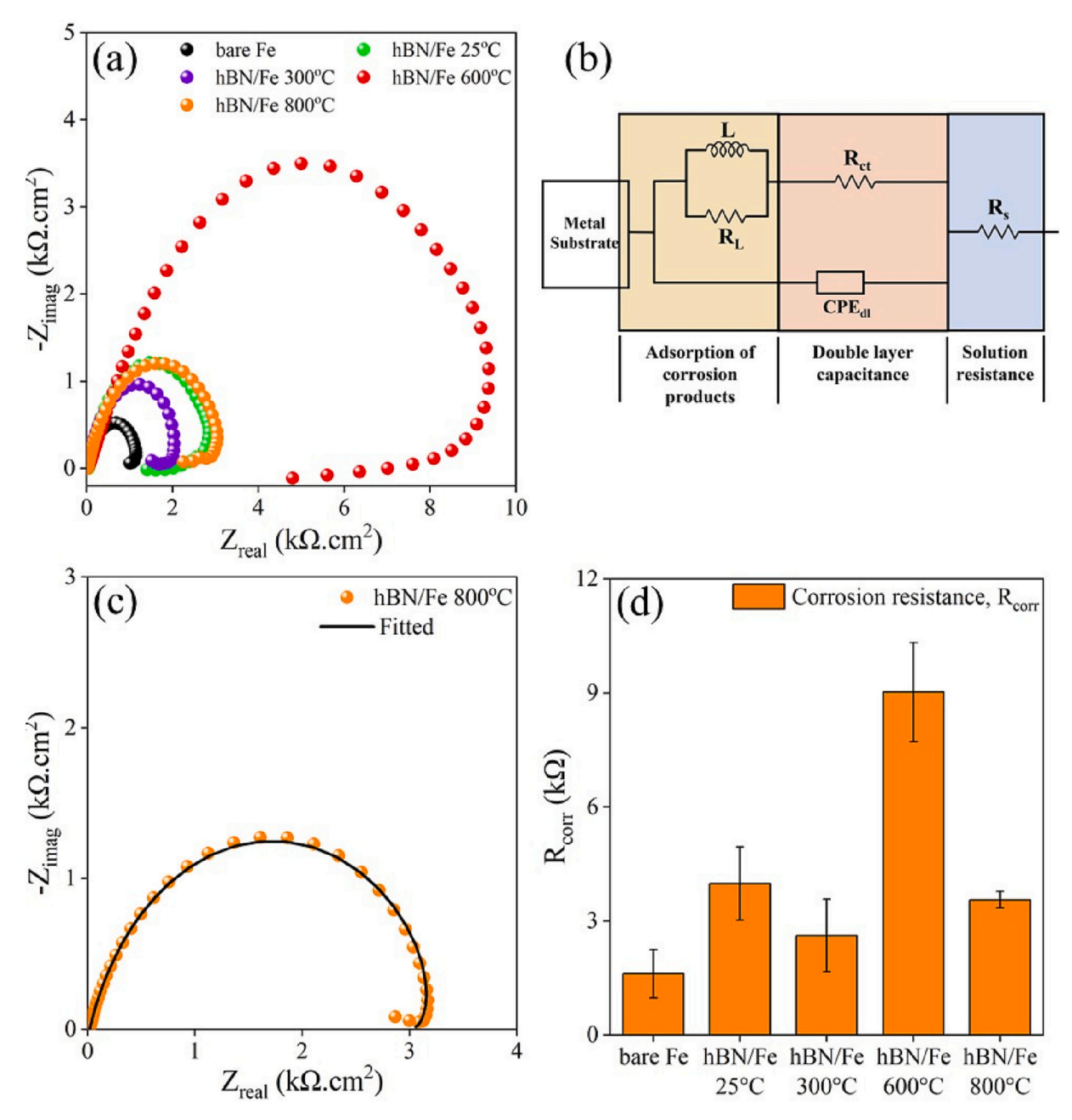


Fig. 12. Electrochemical measurements of coated and uncoated Fe substrates with exposure to 3.5 wt% NaCl solution showing: (a) Nyquist plots of bare and coated Fe substrates as a function of deposition temperature; (b) EEC model used to fit all the samples; (c) Nyquist plot and fitted data of hBN/Fe deposited at 800 °C; and (d) corrosion resistance of hBN coated and uncoated Fe substrates at different deposition temperatures.

systems as well in the literature [89,90].

3.6. Corrosion behavior of hBN nanocoatings deposited on Fe substrates

Corrosion behavior of bare Fe and hBN coated Fe substrates was evaluated in 3.5 wt% NaCl solution. Open circuit potential (OCP) is considered as a preliminary step to understand the corrosion resistance of a material. The relative differences in the potentials between the materials will provide an understanding of the stability of the materials in the corrosion environments. Material with relatively higher potential is considered more noble and thermodynamically stable than material with lower potential. Fig. S13 shows the results of OCP analysis performed, before EIS and Tafel analysis, on bare and hBN/Fe substrates for 60 min. The results indicate that the hBN/Fe deposited at 600 °C with a thickness of ~115 nm shows a more noble potential of -420 mV compared to all the samples. Fig. 12a shows the EIS response (Nyquist plots) of hBN coated and uncoated Fe substrates at room temperature. The Bode plots of bare and hBN coated Fe substrates are shown in the supplementary information, Fig. S14. The magnitude of Nyquist loops (i. e., polarization resistance R_p) provides information on the corrosion resistance of the samples. The higher the loop radii, the higher the R_p; hence, corrosion resistance is higher. The hBN coated Fe substrates show higher loop radii than bare Fe substrates. Therefore, hBN coated substrates have higher corrosion resistance than bare Fe. Among the hBN coated substrates, hBN/Fe deposited at 600 °C showed higher corrosion resistance as loop radii were almost ~3 times higher than others (and also ~8 times higher than bare Fe). Table 2 shows the EIS parameters fitted with the simulated EEC model constructed by the response from EIS plots. As observed from Nyquist plots, a semicircle is well-defined at higher and medium frequencies corresponding to the capacitive loops, and an inductive loop is found at low-frequency regions. Capacitive loops represent the resistance-capacitance behavior at the metal electrolyte interface (double layer). Inductive loops correspond to the relaxation of intermediate species (adsorption of corrosion products) formed on the surface of the electrode as a result of dissolution, frequently observed in steels undergoing rapid corrosion processes [91-94]. Impedance spectra follow a one-time constant, and an inductor connected in series with solution resistance, as depicted in Fig. 12b. In the EEC model, shown in Fig. 12b, R_s represents the solution resistance, R_{ct} represents the charge transfer resistance of the double layer, CPE_{dl} represents the time constant of the double layer, L represents the inductive behavior, and R_L represents the resistance due to inductance. A similar EEC model was used in previously reported literature on steels [91,92,94] with or without corrosion inhibitors. EEC fitted Nyquist plots of hBN/Fe at different deposition temperatures were shown in supplementary information, Fig. S15.

Fig. 12d represents the corrosion resistance R_{corr} of bare Fe and hBN/Fe deposited at different deposition temperatures. $R_{corr}=R_{ct}+R_L$ gives the overall corrosion resistance, as resistances R_L and R_{ct} are connected in series. The hBN coatings on Fe provided improved R_{corr} compared to bare Fe substrate at all deposition temperatures. The hBN/Fe coatings deposited at 25 °C, 300 °C, and 800 °C showed higher R_{corr} of at least $\sim\!1.6\text{--}2.5$ times that of bare Fe. Of all the samples, the hBN/Fe deposited at 600 °C showed the highest R_{corr} of $9.03\pm1.31~k\Omega.cm^2$, which is at least $\sim\!5.6$ times higher than the bare Fe $(1.61\pm0.64~k\Omega.cm^2)$. These

differences in R_{corr} of hBN thin films can be attributed to poor adhesion, resulting in defects and pores in the deposited hBN films (except at 600 °C), providing a pathway for the diffusion of corrosive ions reaching the Fe surface (as shown in Figs. S8, S9, S10).

The double-layer capacitance (C_{dl}) is determined from the time constant CPE_{dl} using Eq. (1) [95,96].

$$C_{dl} = Q / \left(R_{ct}^{-1}\right)^{1-\alpha} \tag{1}$$

Where Q is the constant phase element (CPE), and α is the CPE exponent. The parameters Q and α are determined by fitting EEC models to Nyquist plots. hBN coated Fe substrate show lower C_{dl} than bare Fe (Table 2). The lowest value of C_{dl} of $225\pm46~\mu\text{F/cm}^2$ is observed for hBN/Fe deposited at 600~C, which is almost ~ 5 times lower than the bare ones $(1225\pm357~\mu\text{F/cm}^2)$, indicating that hBN film impeding the pathway of aggressive ions from contacting the Fe substrate. The inhibition efficiency (IE) of hBN-coated substrates was calculated from R_{corr} values determined from EIS analysis using Eq. (2) and is listed in Table 2. The results showed that IE of hBN/Fe made at 600~C was as high as 82 %, followed by 59 % at 25 °C, 55 % at 800 °C and 38 % at 300 °C. Therefore, the overall EIS results suggest that hBN/Fe deposited at 600~C exhibited higher corrosion resistance, lower double-layer capacitance, and an IE of 82 %, indicating the strong barrier coating ability to inhibit the corrosion activity of Fe substrate.

$$IE = \frac{R_{corr,coated} - R_{corr,bare}}{R_{corr,coated}} * 100$$
 (2)

Where $R_{corr,coated}$ is corrosion resistance of hBN coated Fe substrate and $R_{corr,bare}$ is corrosion resistance of bare/uncoated Fe substrate.

Additionally, electrochemical activity of hBN coated and bare Fe substrates was analyzed using potentiodynamic polarization curves (Tafel plots), and the relative comparison is shown in Fig. 13a,b. The corrosion parameters (corrosion rate (CR) along with E_{corr} and I_{corr}) determined from Tafel plots are summarized in Tables 3 and 4. Fig. 13c, d shows the corrosion rates of hBN coated/uncoated Fe substrates at different deposition temperatures and coating thicknesses. Of all the samples, hBN/Fe deposited at 600 $^{\circ}\text{C}$ with a thickness of 115 nm comparably showed lower corrosion rates (and showed lower I_{corr} and noble E_{corr}).

There is clear evidence from Table 3 that hBN/Fe deposited at temperatures ${\geq}600~^{\circ}\text{C}$ showed reduced I_{corr} than others. Almost no significant differences in the I_{corr} of 3.27–3.33 $\mu\text{A/cm}^2$ were observed for bare Fe, and hBN/Fe deposited at 25 $^{\circ}\text{C}$, and 300 $^{\circ}\text{C}$. This indicates the presence of defects (e.g., cracking, delamination) in hBN films (deposited at 25 $^{\circ}\text{C}$, and 300 $^{\circ}\text{C}$) could have created diffusion pathways for ions/molecules through the hBN nanocoating reaching the substrate, resulting in a subsequent electrochemical activity. As deposition temperatures increased to ${\geq}600~^{\circ}\text{C}$, the I_{corr} significantly reduced to 0.72 $\pm0.10~\mu\text{A/cm}^2$ at 600 $^{\circ}\text{C}$ and 1.03±0.51 $\mu\text{A/cm}^2$ at 800 $^{\circ}\text{C}$. This drop in I_{corr} suggests that the hBN coating is comparably intact and providing a corrosion barrier for the Fe substrate. It is well known that current density is directly proportional to corrosion rates, and current density and corrosion rates follow a similar trend, as evident from Table 3.

No significant changes in the CR were observed for bare Fe, hBN/Fe deposited at 25 °C and 300 °C, as shown in Fig. 13c. The average corrosion rates were in the range of $38.91–39.59~\mu m/y$. The hBN/Fe

Table 2
Corrosion parameters, determined from EIS plots of 115 nm thick hBN coated/uncoated substrates at different deposition temperatures.

Samples	$R_s (\Omega.cm^2)$	$R_{ct} (k\Omega.cm^2)$	$R_L (k\Omega.cm^2)$	R_{corr} (k Ω .cm ²) ($R_{ct} + R_{L}$)	C _{dl} (μF/cm ²)	Inhibition efficiency (%)
bare Fe	27 ± 8	1.27 ± 0.51	0.35 ± 0.15	1.61 ± 0.64	1225 ± 357	
hBN/Fe 25 °C	26 ± 9	3.00 ± 0.66	0.99 ± 0.48	3.99 ± 0.96	323 ± 79	59.5
hBN/Fe 300 °C	19 ± 2	1.63 ± 0.54	0.99 ± 0.42	2.62 ± 0.96	521 ± 72	38.4
hBN/Fe 600 °C	37 ± 7	6.85 ± 1.07	2.18 ± 0.40	9.03 ± 1.31	225 ± 46	82.1
hBN/Fe 800 °C	23 ± 3	2.71 ± 0.33	0.86 ± 0.30	3.56 ± 0.22	615 ± 172	54.7

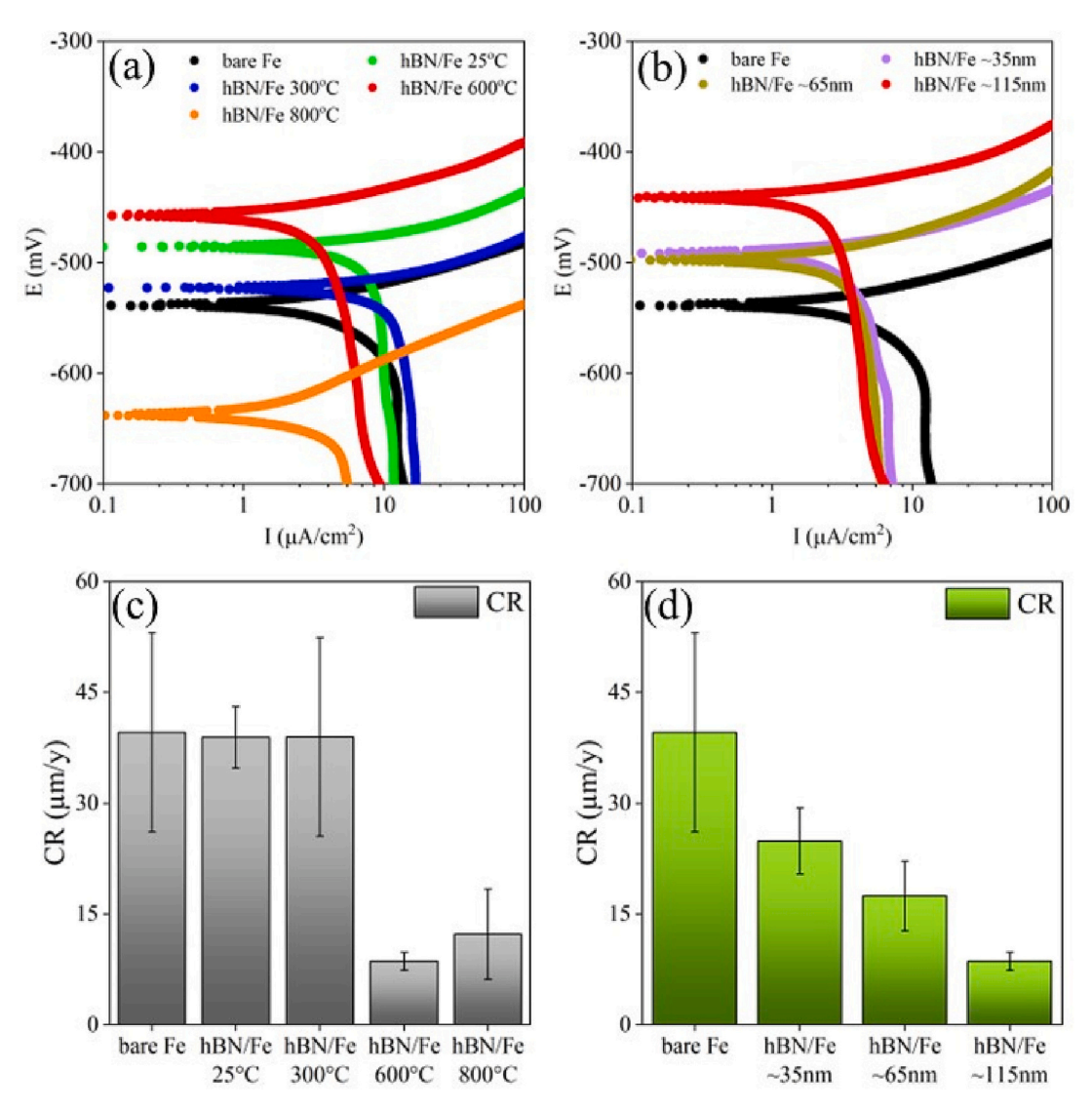


Fig. 13. Potentiodynamic polarization measurements of hBN nanocoatings showing: (a, b) comparison of Tafel plots of bare Fe and hBN coated Fe at various deposition temperatures and coating thicknesses; (c, d) corrosion rates of bare and hBN coated Fe deposited at different deposition temperatures and thicknesses, respectively.

 $\begin{tabular}{ll} \textbf{Table 3} \\ \textbf{Corrosion parameters, determined from Tafel plots, of hBN coated/uncoated} \\ \textbf{Substrates with thickness 115 nm at different deposition temperatures.} \\ \end{tabular}$

Samples	E _{corr} (mV)	$I_{corr} (\mu A/cm^2)$	CR (µm/y)
bare Fe	-537 ± 30	3.33 ± 1.33	39.59 ± 13.46
hBN/Fe 25 °C	-481 ± 6	3.27 ± 0.35	38.91 ± 4.17
hBN/Fe 300 °C	-550 ± 19	3.28 ± 1.13	38.96 ± 13.54
hBN/Fe 600 °C	-444 ± 10	0.72 ± 0.10	8.58 ± 1.23
hBN/Fe 800 °C	-612 ± 21	1.03 ± 0.51	12.24 ± 6.08

Table 4 Corrosion parameters, determined from Tafel plots, of hBN coated/uncoated substrates deposited at 600 $^{\circ}$ C with different thicknesses.

Samples	E _{corr} (mV)	$I_{corr} (\mu A/cm^2)$	CR (µm/y)
bare Fe hBN/Fe 35 nm	-537 ± 30 -493 ± 28	3.33 ± 1.33 2.10 ± 1.33	38.59 ± 13.46 24.89 ± 4.49
hBN/Fe 65 nm hBN/Fe 115 nm	$-488 \pm 24 \\ -444 \pm 10$	$\begin{array}{c} 1.47 \pm 0.40 \\ 0.72 \pm 0.10 \end{array}$	$17.44 \pm 4.70 \\ 8.58 \pm 1.23$

made at 600 °C shows a lower CR of $8.58\pm1.23~\mu\text{m/y}$, a reduction of ~4.6 times, followed by hBN/Fe at 800 °C with $12.24\pm6.08~\mu\text{m/y}$, a reduction of ~3.3 times compared to that of bare Fe. Though the hBN/Fe made at 800 °C reported lower I_{corr} and CR compared to bare Fe, the coatings showed indications of cracking in a few locations, as shown in supplementary information Fig. S10, which resulted in non-uniform coatings, and hence, high standard deviations of current densities and corrosion rates were observed. The overall corrosion testing showed that the hBN thin films deposited at 600 °C had a more noble electrochemical potential, and lower corrosion rates. These results were also in excellent agreement with the EIS data, which showed higher corrosion resistance and lower double-layer capacitance for hBN/Fe thin films deposited at 600 °C.

As the deposition temperature of 600 °C yielded higher corrosion resistance (from EIS) and lower corrosion rates (from Tafel), the effect of hBN film thickness on corrosion properties was investigated at the same temperature. The E_{corr} of hBN/Fe deposited at 600 °C with varying thicknesses showed noble potentials compared to bare Fe, as evident from Table 4. The E_{corr} of hBN/Fe made at 600 °C increased from $-493\,\pm28$ mV with 35 nm thickness to -488 ± 24 mV with a thickness of 65 nm and -444 ± 10 mV with a thickness of 115 nm. And the I_{corr} of hBN/Fe decreased with various thicknesses compared to bare Fe. The I_{corr} of

hBN films decreased from $2.10\pm1.33~\mu\text{A/cm}^2$ with a thickness of 35 nm to $1.47\pm0.40~\mu\text{A/cm}^2$ with a thickness of 65 nm and $0.72\pm0.10~\mu\text{A/cm}^2$ with a thickness of 115 nm. With the increase in the hBN film thickness on the Fe substrate, an increase in Ecorr and a decrease in Icorr of the coatings were observed, implying a thicker barrier coating is needed for better corrosion protection. Fig. 13d shows that the hBN coatings deposited at 600 °C, irrespective of thickness, showed lower corrosion rates than bare Fe. However, the corrosion rates decreased with an increase in the thickness of hBN coatings, from $24.89\pm4.49~\mu\text{m/y}$ (a reduction of ~ 1.6 times) for 35 nm thickness to 17.44 ± 4.70 $\mu m/y$ (a reduction of ${\sim}2.3$ times) for 65 nm thickness and $8.58{\pm}1.23~\mu\text{m/y}$ (a reduction of ~4.6 times) for 115 nm thickness. In the end, the hBN/Fe deposited at 600 °C with a thickness of 115 nm showed the lowest corrosion rates among all samples, indicating a promising candidate for strong corrosion resistance coating for inhibiting corrosion in aggressive saline environments.

Additional SEM/EDS analysis was performed to analyze corrosion products formed on the samples after Tafel analysis, shown in supplementary information Fig. S16. The results (of bare Fe and hBN/Fe deposited at 25 °C) indicate the presence of an oxygen peak after electrochemical measurements due to the corrosion activity of Fe. Similar results are observed in all the post-corrosion samples. The published literature on corrosion properties of hBN thin films developed by physical vapor deposition processes has been very limited. Tang et al. [38] reported ~3 times reduction in the corrosion rate of 200 nm thick hBN films on stainless steel (SS) substrates (hBN/SS $-0.05 \mu m/y$, and bare SS $-0.14 \,\mu\text{m/y}$). Kumar et al. [36] showed that the corrosion rate of \sim 1 µm thick pulsed laser deposited hBN film on SS (11.68 µm/y) was reduced by \sim 23 times compared to bare SS (279.40 μ m/y). Compared to the reported literature, in this study, the corrosion rate of the underlying Fe substrate was decreased by ~4.6 times with a hBN coating thickness of 115 nm.

This study successfully demonstrated the growth of hBN nanocoatings on Fe substrates using the PLD technique. We found that 115 nm thick hBN coatings deposited at 600 °C showed the best corrosion protection by providing excellent chemical stability in salt solutions, and significantly lower corrosion rates. Lower corrosion rates of hBN coatings indicated longer protection life of underlying Fe substrate. Based on the results from electrochemical studies, the schematic illustration of the corrosive mechanism involved in the bare and hBN coated Fe substrates was presented (as shown in Fig. 14). The corrosion of Fe substrate exposed to aggressive NaCl solution involves a few steps [36,97]: initially, Cl⁻ ions dissolved in the electrolyte reacts with the surface of the Fe substrate and form iron chloride FeCl2, and next, this FeCl2 reacts with water and forms Fe(OH)2 and hydrochloric acid. However, in the case of hBN nanocoatings, hBN layers act as a barrier coating and limit the direct contact between the aggressive Cl⁻ ions and the surface of the Fe substrate, hindering the diffusion pathways of ions and molecules, and thereby slowing down the corrosion process. Therefore, the crackfree hBN thin films can be considered as an effective coating material for enhanced corrosion resistance of underlying substrates. Finally, the electrochemical studies confirm that hBN thin films can act as barrier coatings and lowers the corrosion rate of Fe substrates in aggressive saline environments.

4. Conclusions

Developing protective barrier coatings on Fe is essential to minimize the corrosion related environmental impacts. Here, we demonstrated the use of PLD as a nanomanufacturing method to synthesize corrosion resistant hBN nanocoatings directly on iron substrates at different deposition temperatures and thicknesses. Results suggest that deposition temperature and thickness of hBN coatings can greatly influence the film microstructure and corrosion properties. The presence of hBN phase in the deposited coatings was confirmed by Raman, GIXRD and TEM analysis. hBN depositions above 600 °C showed uniform distribution of

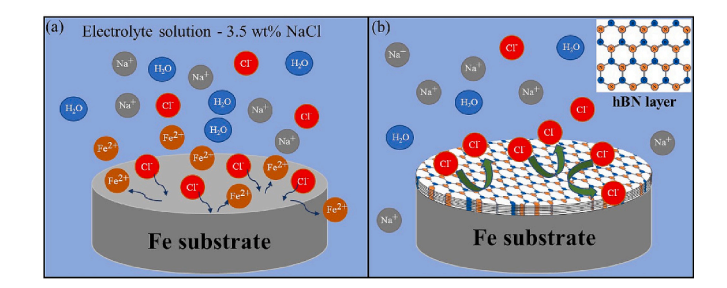


Fig. 14. Schematic illustration of bare and hBN coated Fe substrates exposed to the aggressive corrosive electrolyte (3.5 wt% NaCl solution) showing: (a) corrosion behavior of bare Fe; and (b) anti-corrosion behavior of hBN nanocoating on Fe substrate.

hBN nanocrystallites and improved crystallinity. Surface roughness increased with the deposition temperature and thickness; hence, the contact angle followed the same trend. hBN thin films showed relatively higher hardness and lower modulus compared to bare Fe. Electrochemical studies revealed that the hBN coated Fe substrates made at 600 $^{\circ}\text{C}$ showed better barrier properties with lower corrosion rates, and the corrosion rates decreased with an increase in hBN coating thickness from 35 nm to 115 nm. Corrosion inhibition efficiency of Fe was improved by 82 % with deposition of 115 nm thick hBN. Therefore, the hBN nanocoatings can serve as protective barrier coatings in aggressive environments and can potentially be used for various material coating applications.

Funding

This work was supported by National Science Foundation awards (grant numbers #1849206 and #1920954).

CRediT authorship contribution statement

Venkata A.S. Kandadai: Conceptualization, Methodology, Investigation, Visualization, Writing – original draft. Jacob B. Petersen: Methodology, Visualization, Writing – review & editing. Venkataramana Gadhamshetty: Validation, Resources, Writing – review & editing, Funding acquisition. Bharat K. Jasthi: Supervision, Project administration, Conceptualization, Methodology, Visualization, Writing – review & editing, Funding acquisition.

Declaration of competing interest

The authors declare that they have no known competing financial interests or personal relationships that could have appeared to influence the work reported in this paper.

Data availability

Data will be made available on request.

Acknowledgements

The authors would like to acknowledge the funding support from National Science Foundation awards (RII Track-1: Building on the 2020 Vision: Expanding Research, Education, and Innovation in SD (#1849206) and RII Track-2 FEC: Data Driven Material Discovery Center for Bioengineering Innovation (#1920954). We acknowledge the contributions of Dr. Suvarna Talluri towards initial installation of the PLD equipment.

Appendix A. Supplementary data

Supplementary data to this article can be found online at https://doi.org/10.1016/j.surfcoat.2023.129736.

References

- [1] C. Verma, E.E. Ebenso, M. Quraishi, Corrosion inhibitors for ferrous and non-ferrous metals and alloys in ionic sodium chloride solutions: a review, J. Mol. Liq. 248 (2017) 927–942.
- [2] I. Ore, I. Pigments, P. Rock, Q. Crystal, R. Earths, S. Ash, Mineral Commodity Summaries 2021: Nitrogen, (Fixed)-Ammonia, 2021.
- [3] E. Husain, T.N. Narayanan, J.J. Taha-Tijerina, S. Vinod, R. Vajtai, P.M. Ajayan, Marine corrosion protective coatings of hexagonal boron nitride thin films on stainless steel, ACS Appl. Mater. Interfaces 5 (2013) 4129–4135.
- [4] I. Stojanović, V. Šimunović, V. Alar, F. Kapor, Experimental evaluation of polyester and epoxy–polyester powder coatings in aggressive media, Coatings 8 (2018) 98.
- [5] M. Ates, A review on conducting polymer coatings for corrosion protection, J. Adhes. Sci. Technol. 30 (2016) 1510–1536.
- [6] F. Beck, Electrodeposition of polymer coatings, Electrochim. Acta 33 (1988)
- [7] R. Hasanov, S. Bilgiç, Monolayer and bilayer conducting polymer coatings for corrosion protection of steel in 1 M H2SO4 solution, Progress in Organic Coatings 64 (2009) 435–445.
- [8] T. Rout, G. Jha, A. Singh, N. Bandyopadhyay, O. Mohanty, Development of conducting polyaniline coating: a novel approach to superior corrosion resistance, Surf. Coat. Technol. 167 (2003) 16–24.
- [9] M. Kendig, M. Hon, L. Warren, Smart'corrosion inhibiting coatings, Progress in Organic Coatings 47 (2003) 183–189.
- [10] A.U. Ammar, M. Shahid, M.K. Ahmed, M. Khan, A. Khalid, Z.A. Khan, Electrochemical study of polymer and ceramic-based nanocomposite coatings for corrosion protection of cast iron pipeline, Materials 11 (2018) 332.
- [11] T. Peng, R. Xiao, Z. Rong, H. Liu, Q. Hu, S. Wang, X. Li, J. Zhang, Polymer nanocomposite-based coatings for corrosion protection, Chemistry–An Asian Journal 15 (2020) 3915–3941.
- [12] A. Olad, A. Rashidzadeh, M. Amini, Preparation of polypyrrole nanocomposites with organophilic and hydrophilic montmorillonite and investigation of their corrosion protection on iron, Adv. Polym. Technol. 32 (2013).
- [13] A. Olad, M. Barati, S. Behboudi, Preparation of PANI/epoxy/Zn nanocomposite using Zn nanoparticles and epoxy resin as additives and investigation of its corrosion protection behavior on iron, Progress in Organic Coatings 74 (2012) 221–227.
- [14] N. Attarzadeh, M. Molaei, K. Babaei, A. Fattah-alhosseini, New promising ceramic coatings for corrosion and wear protection of steels: a review, Surfaces and Interfaces 23 (2021), 100997.
- [15] Y. Wang, Z. Jiang, Z. Yao, H. Tang, Microstructure and corrosion resistance of ceramic coating on carbon steel prepared by plasma electrolytic oxidation, Surf. Coat. Technol. 204 (2010) 1685–1688.
- [16] G. Shen, Y. Chen, L. Lin, C. Lin, D. Scantlebury, Study on a hydrophobic nano-TiO2 coating and its properties for corrosion protection of metals, Electrochim. Acta 50 (2005) 5083–5089.
- [17] A. Anderson, Corrosion resistance of ceramic coatings sprayed on stainless steel substrates, International Journal of Ambient Energy 38 (2017) 320–322.
- [18] G. Chilkoor, N. Shrestha, S.P. Karanam, V.K. Upadhyayula, V. Gadhamshetty, Graphene Coatings for Microbial Corrosion Applications, Encyclopedia of Water, Science, Technology, and Society, 2019, pp. 1–25.
- [19] T. Arai, S. Harper, Thermoreactive deposition/diffusion process, ASM International, ASM Handbook. 4 (1991) 448–453.
- [20] A. Günen, E. Kanca, H. Çakir, M.S. Karakaş, M.S. Gök, Y. Küçük, M. Demir, Effect of borotitanizing on microstructure and wear behavior of Inconel 625, Surf. Coat. Technol. 311 (2017) 374–382.
- [21] A. Günen, Y. Kanca, İ.H. Karahan, M.S. Karakaş, M.S. Gök, E. Kanca, A. Çürük, A comparative study on the effects of different thermochemical coating techniques on corrosion resistance of STKM-13A steel, Metall. Mater. Trans. A 49 (2018) 5833–5847
- [22] D. Kumaravel, K. Arunkumar, in: Advances in Manufacturing Processes: Select Proceedings of ICEMMM 2018, Springer, 2019, pp. 123–131.
- [23] E.J. Mittemeijer, M.A. Somers, Thermochemical Surface Engineering of Steels, Woodhead Publishing Cambridge, 2014.
- [24] A. Biserova-Tahchieva, J.M. Cabrera, N. Llorca-Isern, Study of the thermochemical surface treatment effect on the phase precipitation and degradation behaviour of DSS and SDSS, Materials 13 (2020) 165.
- [25] J. Islam, P.K. Obulisamy, V.K. Upadhyayula, A.B. Dalton, P.M. Ajayan, M. M. Rahman, M. Tripathi, R.K. Sani, V. Gadhamshetty, Graphene as Thinnest Coating on Copper Electrodes in Microbial Methanol Fuel Cells, ACS nano, 2022.
- [26] A. Krishnamurthy, V. Gadhamshetty, R. Mukherjee, B. Natarajan, O. Eksik, S. Ali Shojaee, D.A. Lucca, W. Ren, H.-M. Cheng, N. Koratkar, Superiority of graphene over polymer coatings for prevention of microbially induced corrosion, Sci. Rep. 5 (2015) 1–12.
- [27] A. Krishnamurthy, V. Gadhamshetty, R. Mukherjee, Z. Chen, W. Ren, H. Cheng, N. Koratkar, Passivation of microbial corrosion using a graphene coating, Carbon 56 (2013) 45–49.
- [28] G. Chilkoor, R. Sarder, J. Islam, K. ArunKumar, I. Ratnayake, S. Star, B.K. Jasthi, G. Sereda, N. Koratkar, M. Meyyappan, Maleic anhydride-functionalized graphene

- nanofillers render epoxy coatings highly resistant to corrosion and microbial attack, Carbon 159 (2020) 586–597.
- [29] Y. Wu, X. Zhu, W. Zhao, Y. Wang, C. Wang, Q. Xue, Corrosion mechanism of graphene coating with different defect levels, J. Alloys Compd. 777 (2019) 135-144.
- [30] M. Schriver, W. Regan, W.J. Gannett, A.M. Zaniewski, M.F. Crommie, A. Zettl, Graphene as a long-term metal oxidation barrier: worse than nothing, ACS Nano 7 (2013) 5763–5768.
- [31] F. Zhou, Z. Li, G.J. Shenoy, L. Li, H. Liu, Enhanced room-temperature corrosion of copper in the presence of graphene, ACS Nano 7 (2013) 6939–6947.
- [32] G. Chilkoor, K. Jawaharraj, B. Vemuri, A. Kutana, M. Tripathi, D. Kota, T. Arif, T. Filleter, A.B. Dalton, B.I. Yakobson, M. Meyyappan, M.M. Rahman, P.M. Ajayan, V. Gadhamshetty, Hexagonal boron nitride for sulfur corrosion inhibition, ACS Nano 14 (2020) 14809–14819.
- [33] G. Chilkoor, S.P. Karanam, S. Star, N. Shrestha, R.K. Sani, V.K.K. Upadhyayula, D. Ghoshal, N.A. Koratkar, M. Meyyappan, V. Gadhamshetty, Hexagonal boron nitride: the thinnest insulating barrier to microbial corrosion, ACS Nano 12 (2018) 2242–2252.
- [34] K.K. Kim, A. Hsu, X. Jia, S.M. Kim, Y. Shi, M. Hofmann, D. Nezich, J.F. Rodriguez-Nieva, M. Dresselhaus, T. Palacios, Synthesis of monolayer hexagonal boron nitride on cu foil using chemical vapor deposition, Nano Lett. 12 (2012) 161–166.
- [35] F. Mahvash, S. Eissa, T. Bordjiba, A.C. Tavares, T. Szkopek, M. Siaj, Corrosion resistance of monolayer hexagonal boron nitride on copper, Sci. Rep. 7 (2017) 42139.
- [36] A. Kumar, G. Malik, M.K. Pandey, R. Chandra, R.S. Mulik, Corrosion behavior of pulse laser deposited 2D nanostructured coating prepared by self-made h-BN target in salinity environment, Ceram. Int. 47 (2021) 12537–12546.
- [37] M. Singh, H. Vasudev, R. Kumar, Corrosion and Tribological behaviour of BN thin films deposited using magnetron sputtering, International Journal of Surface Engineering and Interdisciplinary Materials Science (IJSEIMS) 9 (2021) 24–39.
- [38] X. Tang, H. Wang, C. Liu, X. Zhu, W. Gao, H. Yin, Direct growth of hexagonal boron nitride Nanofilms on stainless steel for corrosion protection, ACS Applied Nano Materials 4 (2021) 12024–12033.
- [39] A. Pakdel, C. Zhi, Y. Bando, T. Nakayama, D. Golberg, Boron nitride nanosheet coatings with controllable water repellency, ACS Nano 5 (2011) 6507–6515.
 [40] D. Akinwande, N. Petrone, J. Hone, Two-dimensional flexible nanoelectronics, Nat.
- [40] D. Akinwande, N. Petrone, J. Hone, Two-dimensional flexible nanoelectronics, Nat. Commun. 5 (2014) 5678.
- [41] C.R. Dean, A.F. Young, I. Meric, C. Lee, L. Wang, S. Sorgenfrei, K. Watanabe, T. Taniguchi, P. Kim, K.L. Shepard, J. Hone, Boron nitride substrates for highquality graphene electronics, Nat. Nanotechnol. 5 (2010) 722–726.
- [42] K.K. Kim, A. Hsu, X. Jia, S.M. Kim, Y. Shi, M. Dresselhaus, T. Palacios, J. Kong, Synthesis and characterization of hexagonal boron nitride film as a dielectric layer for graphene devices, ACS Nano 6 (2012) 8583–8590.
- [43] J. Xue, J. Sanchez-Yamagishi, D. Bulmash, P. Jacquod, A. Deshpande, K. Watanabe, T. Taniguchi, P. Jarillo-Herrero, B.J. LeRoy, Scanning tunnelling microscopy and spectroscopy of ultra-flat graphene on hexagonal boron nitride, Nat. Mater. 10 (2011) 282–285.
- [44] Z. Zhang, X.C. Zeng, W. Guo, Fluorinating hexagonal boron nitride into diamond-like nanofilms with tunable band gap and ferromagnetism, J. Am. Chem. Soc. 133 (2011) 14831–14838.
- [45] L. Song, L. Ci, H. Lu, P.B. Sorokin, C. Jin, J. Ni, A.G. Kvashnin, D.G. Kvashnin, J. Lou, B.I. Yakobson, P.M. Ajayan, Large scale growth and characterization of atomic hexagonal boron nitride layers, Nano Lett. 10 (2010) 3209–3215.
- [46] A. Ismach, H. Chou, D.A. Ferrer, Y. Wu, S. McDonnell, H.C. Floresca, A. Covacevich, C. Pope, R. Piner, M.J. Kim, R.M. Wallace, L. Colombo, R.S. Ruoff, Toward the controlled synthesis of hexagonal boron nitride films, ACS Nano 6 (2012) 6378–6385.
- [47] Y. Shi, C. Hamsen, X. Jia, K.K. Kim, A. Reina, M. Hofmann, A.L. Hsu, K. Zhang, H. Li, Z.Y. Juang, M.S. Dresselhaus, L.J. Li, J. Kong, Synthesis of few-layer hexagonal boron nitride thin film by chemical vapor deposition, Nano Lett. 10 (2010) 4134–4139.
- [48] S. Caneva, M.-B. Martin, L. D'Arsié, A.I. Aria, H. Sezen, M. Amati, L. Gregoratti, H. Sugime, S. Esconjauregui, J. Robertson, From growth surface to device interface: preserving metallic Fe under monolayer hexagonal boron nitride, ACS Appl. Mater. Interfaces 9 (2017) 29973–29981.
- [49] S. Jia, W. Chen, J. Zhang, C.-Y. Lin, H. Guo, G. Lu, K. Li, T. Zhai, Q. Ai, J. Lou, CVD growth of high-quality and large-area continuous h-BN thin films directly on stainless-steel as protective coatings, Materials Today Nano 16 (2021), 100135.
- [50] J. Meng, X. Zhang, Y. Wang, Z. Yin, H. Liu, J. Xia, H. Wang, J. You, P. Jin, D. Wang, Aligned growth of millimeter-size hexagonal boron nitride single-Crystal domains on epitaxial nickel thin film, Small 13 (2017) 1604179.
- [51] H. Park, T.K. Kim, S.W. Cho, H.S. Jang, S.I. Lee, S.-Y. Choi, Large-scale synthesis of uniform hexagonal boron nitride films by plasma-enhanced atomic layer deposition, Sci. Rep. 7 (2017) 1–8.
- [52] V.A. Kandadai, V. Gadhamshetty, B.K. Jasthi, Effect of buffer layer and substrate growth temperature on the microstructural evolution of hexagonal boron nitride thin films, Surf. Coat. Technol. 447 (2022), 128805.
- [53] N. Acacia, E. Fazio, F. Neri, P.M. Ossi, S. Trusso, N. Santo, Pulsed laser deposition of boron nitride thin films, Radiation Effects & Defects in Solids 163 (2008) 293–298.
- [54] P. Willmott, J. Huber, Pulsed laser vaporization and deposition, Rev. Mod. Phys. 72 (2000) 315.
- [55] C. Ramana, K. Zaghib, C. Julien, Synthesis, structural and electrochemical properties of pulsed laser deposited Li (Ni, co) O2 films, J. Power Sources 159 (2006) 1310–1315.

- [56] O. Hussain, K. Srinivasa Rao, K. Madhuri, C. Ramana, B. Naidu, S. Pai, J. John, R. Pinto, Growth and characteristics of reactive pulsed laser deposited molybdenum trioxide thin films, Applied Physics A 75 (2002) 417–422.
- [57] J. Giapintzakis, C. Grigorescu, A. Klini, A. Manousaki, V. Zorba, J. Androulakis, Z. Viskadourakis, C. Fotakis, Low-temperature growth of NiMnSb thin films by pulsed-laser deposition, Applied Physics Letters 80 (15) (2002) 2716–2718.
- [58] C. Ramana, O. Hussain, R. Pinto, C. Julien, Microstructural features of pulsed-laser deposited V2O5 thin films, Appl. Surf. Sci. 207 (2003) 135–138.
- [59] K. Wang, G. Tai, K. Wong, S.P. Lau, W. Guo, Ni induced few-layer graphene growth at low temperature by pulsed laser deposition, AIP Adv. 1 (2011), 022141.
- [60] S.H. Lee, T.K. Song, T. Noh, J.H. Lee, Low-temperature growth of epitaxial LiNbO3 films on sapphire (0001) substrates using pulsed laser deposition, Appl. Phys. Lett. 67 (1995) 43–45.
- [61] G. Pharr, W. Oliver, Measurement of thin film mechanical properties using nanoindentation, MRS Bull. 17 (1992) 28–33.
- [62] W.C. Oliver, G.M. Pharr, An improved technique for determining hardness and elastic modulus using load and displacement sensing indentation experiments, J. Mater. Res. 7 (1992) 1564–1583.
- [63] T. Han, Y. Luo, C. Wang, Effects of temperature and strain rate on the mechanical properties of hexagonal boron nitride nanosheets, J. Phys. D. Appl. Phys. 47 (2013), 025303.
- [64] Q. Peng, W. Ji, S. De, Mechanical properties of the hexagonal boron nitride monolayer: ab initio study, Comput. Mater. Sci. 56 (2012) 11–17.
- [65] W. Köster, H. Franz, Poisson's ratio for metals and alloys, Metallurgical reviews 6
- [66] M.A. Baba, A. Gasim, A.M. Awadelgied, N.A. Almuslet, A.M. Salih, Influence of the annealing temperature on the thickness and roughness of La 2 Ti 2 O 7 thin films, Advances in Materials Physics and Chemistry 10 (2020) 189.
- [67] C. Mahajan, M. Takwale, An influence of deposition temperature on structural, optical and electrical properties of sprayed ZnO thin films of identical thickness, Curr. Appl. Phys. 13 (2013) 2109–2116.
- [68] L. Schué, I. Stenger, F. Fossard, A. Loiseau, J. Barjon, Characterization methods dedicated to nanometer-thick hBN layers, 2D Materials 4 (2016), 015028.
- [69] I. Stenger, L. Schué, M. Boukhicha, B. Berini, B. Plaçais, A. Loiseau, J. Barjon, Low frequency Raman spectroscopy of few-atomic-layer thick hBN crystals, 2D Materials 4 (2017), 031003.
- [70] U. Chandni, K. Watanabe, T. Taniguchi, J. Eisenstein, Evidence for defect-mediated tunneling in hexagonal boron nitride-based junctions, Nano Lett. 15 (2015) 7329–7333.
- [71] Y. Li, V. Garnier, P. Steyer, C. Journet, B. Toury, Millimeter-scale hexagonal boron nitride single crystals for nanosheet generation, ACS Applied Nano Materials 3 (2020) 1508–1515.
- [72] S.J. Barrington, T. Bhutta, D. Shepherd, R.W. Eason, The effect of particulate density on performance of Nd: Gd3Ga5O12 waveguide lasers grown by pulsed laser deposition, Opt. Commun. 185 (2000) 145–152.
- [73] B.A. Movchan, A. Demchishin, Structure and properties of thick condensates of nickel, titanium, tungsten, aluminum oxides, and zirconium dioxide in vacuum, Fiz. Metal. Metalloved. 28: 653–60 (Oct 1969). (1969).
- [74] J. Anderson, Chemisorption and Reactions on Metallic Films V1, Elsevier, 2012.
- [75] J.W. Hutchinson, Stresses and Failure Modes in Thin Films and Multilayers, Notes for a Dcamm Course 1, Technical University of Denmark, Lyngby, 1996, p. 14.
- [76] D. Magnfält, in, Linköping University Electronic Press, 2014.
- [77] L.B. Freund, S. Suresh, Thin Film Materials: Stress, Defect Formation and Surface Evolution, Cambridge University Press, 2004.

- [78] I. Wlasny, P. Dabrowski, M. Rogala, I. Pasternak, W. Strupinski, J. Baranowski, Z. Klusek, Impact of electrolyte intercalation on the corrosion of graphene-coated copper, Corros. Sci. 92 (2015) 69–75.
- [79] M. Tomita, T. Inaguma, H. Sakamoto, K. Ushioda, Recrystallization behavior and texture evolution in severely cold-rolled Fe-0.3 mass% Si and Fe-0.3 mass% Al alloys, ISIJ Int. 57 (2017) 921–928.
- [80] H.E. Cleaves, J. Hiegel, Properties of high-purity iron, J. Res. Natl. Bur. Standards 28 (1942) 1471.
- [81] K. Gocman, T. Kałdoński, W. Mróz, S. Burdyńska, A. Prokopiuk, Structural and mechanical properties of boron nitride thin films deposited on steel substrates by pulsed laser deposition, Journal of KONES 18 (2011) 149–156.
- [82] A. Melaibari, M. Eltaher, High repetition rate deposition of boron nitride films using femtosecond pulsed laser, Materials Research Express 7 (2020), 096401.
- [83] R.N. Wenzel, Resistance of solid surfaces to wetting by water, Industrial & Engineering Chemistry 28 (1936) 988–994.
- [84] E. Wagemann, Y. Wang, S. Das, S.K. Mitra, On the wetting translucency of hexagonal boron nitride, Phys. Chem. Chem. Phys. 22 (2020) 7710–7718.
- [85] X. Li, H. Qiu, X. Liu, J. Yin, W. Guo, Wettability of supported monolayer hexagonal boron nitride in air, Adv. Funct. Mater. 27 (2017) 1603181.
- [86] A. Kumar Verma, A. Govind Rajan, Surface roughness explains the observed water contact angle and slip length on 2D hexagonal boron nitride, Langmuir 38 (2022) 9210, 9220
- [87] A. Govind Rajan, M.S. Strano, D. Blankschtein, Liquids with lower wettability can exhibit higher friction on hexagonal boron nitride: the intriguing role of solid-liquid electrostatic interactions, Nano Lett. 19 (2019) 1539–1551.
- [88] C.H. Lee, J. Drelich, Y.K. Yap, Superhydrophobicity of boron nitride nanotubes grown on silicon substrates, Langmuir 25 (2009) 4853–4860.
- [89] G. Malik, J. Jaiswal, S. Mourya, R. Chandra, Optical and other physical properties of hydrophobic ZnO thin films prepared by dc magnetron sputtering at room temperature, J. Appl. Phys. 122 (2017), 143105.
- [90] K.H. Patel, S.K. Rawal, Contact Angle Hysteresis, Wettability and Optical Studies of Sputtered Zinc Oxide Nanostructured Thin Films, 2017.
- [91] E.-S.M. Sherif, A.T. Abbas, D. Gopi, A. El-Shamy, Corrosion and corrosion inhibition of high strength low alloy steel in 2.0 M sulfuric acid solutions by 3amino-1, 2, 3-triazole as a corrosion inhibitor, Journal of Chemistry, 2014 (2014).
- [92] H.H. Hernández, A.M.R. Reynoso, J.C.T. González, C.O.G. Morán, J.G. M. Hernández, A.M. Ruiz, J.M. Hernández, R.O. Cruz, Electrochemical impedance spectroscopy (EIS): a review study of basic aspects of the corrosion mechanism applied to steels, Electrochemical Impedance Spectroscopy (2020) 137–144.
- [93] S. Yin, H. Yang, Y. Dong, C. Qu, J. Liu, T. Guo, K. Duan, Environmentally favorable magnesium phosphate anti-corrosive coating on carbon steel and protective mechanisms, Sci. Rep. 11 (2021) 197.
- [94] S. Nagarajan, M. Karthega, N. Rajendran, Pitting corrosion studies of super austenitic stainless steels in natural sea water using dynamic electrochemical impedance spectroscopy, J. Appl. Electrochem. 37 (2007) 195–201.
- [95] B. Bera, T. Kar, A. Chakraborty, M. Neergat, Influence of nitrogen-doping in carbon on equivalent distributed resistance and capacitance-implications to electrocatalysis of oxygen reduction reaction, J. Electroanal. Chem. 805 (2017) 184–192.
- [96] R.K. Singh, R. Devivaraprasad, T. Kar, A. Chakraborty, M. Neergat, Electrochemical impedance spectroscopy of oxygen reduction reaction (ORR) in a rotating disk electrode configuration: effect of ionomer content and carbon-support, J. Electrochem. Soc. 162 (2015) F489.
- [97] C.A. Apostolopoulos, S. Demis, V.G. Papadakis, Chloride-induced corrosion of steel reinforcement-mechanical performance and pit depth analysis, Constr. Build. Mater. 38 (2013) 139–146.